

Inflation and Asymmetric Collapse at Kilauea Summit during the 2018 Eruption from Seismic and Infrasond Analyses

Voon Hui Lai^{1,1}, Zhongwen Zhan^{2,2}, Osamu Sandanbata^{3,3}, Quentin Brissaud^{4,4}, and Meghan Samantha Miller^{1,1}

¹Australian National University

²California Institute of Technology

³Now at National Research Institute for Earth Science and Disaster Prevention

⁴Norwegian Seismic Array (NORSAR)

November 30, 2022

Abstract

Characterizing the large M4.7+ seismic events during the 2018 Kilauea eruption is important to understanding the complex subsurface deformation at the Kilauea summit. The first 12 events (May 17 - May 26) are associated with the explosive eruptions and the remaining 50 events (May 29 - August 02) onwards are accompanied by large-scale caldera collapses. It is challenging to resolve their locations and mechanisms because of the shallow source depths, complex velocity structure, and significant non double-couple components. We show the necessity to combine multiple geophysical data including broadband seismometers, accelerometers and infrasond sensors to resolve different aspects of the seismic source. The seismic moment tensor solutions using near-field summit stations show the early events are highly isotropic. Infrasond data and particle motion analysis identify the Halema'uma'u reservoir as the inflation source. For the later collapse events, two independent moment tensor inversions using local and global stations consistently show that asymmetric slips occur on inward-dipping normal faults along the northwest corner of the caldera. Infrasond simulation results suggest there may be inflation during the collapse events although not resolvable seismically. Our findings show that the summit events are characterized by both inflation and asymmetric slip, which are consistent with geodetic data. Based on the location of the slip and microseismicity, the caldera may have failed in a 'see-saw' manner: small continuous slips in the form of microseismicity on the southeast corner of the caldera, compensated by large slips on the northwest during the large collapse events.

1
2 **Inflation and Asymmetric Collapse at Kīlauea Summit**
3 **during the 2018 Eruption from Seismic and Infrasound Analyses**

4 **Voon Hui Lai^{1,2}, Zhongwen Zhan¹,**
5 **Quentin Brissaud^{1,3}, Osamu Sandanbata⁴ and Meghan S. Miller²**

6 ¹Seismological Laboratory, California Institute of Technology, USA.

7 ²Research School of Earth Sciences, The Australian National University, Australia.

8 ³Norwegian Seismic Array (NORSAR), Norway.

9 ⁴National Research Institute for Earth Science and Disaster Resilience, Japan.

10
11 Corresponding author: Voon Hui Lai (voonhui.lai@anu.edu.au)

12
13 **Key Points:**

- 14 • We characterized the large seismic events at the Kīlauea summit using particle motion,
15 infrasound, and seismic moment tensor inversion.
- 16 • Near-field seismic observation is essential to resolve the isotropic contribution due to
17 inflation of the Halema'uma'u reservoir.
- 18 • Two independent moment tensor inversions show that the caldera collapsed
19 asymmetrically along the northwest corner.
20
21

22 **Abstract**

23 Characterizing the large M4.7+ seismic events during the 2018 Kīlauea eruption is
24 important to understand the complex subsurface deformation at the Kīlauea summit. The first 12
25 events (May 17 - May 26) are associated with long-duration seismic signals and the remaining
26 50 events (May 29 - August 02) are accompanied by large-scale caldera collapses. Resolving the
27 source location and mechanism is challenging because of the shallow source depth, significant
28 non double-couple components, and complex velocity structure. We demonstrate that combining
29 multiple geophysical data from broadband seismometers, accelerometers and infrasound is
30 essential to resolve different aspects of the seismic source. Seismic moment tensor solutions
31 using near-field summit stations show the early events are highly volumetric. Infrasound data
32 and particle motion analysis identify the inflation source as the Halema'uma'u reservoir. For the
33 later collapse events, two independent moment tensor inversions using local and global stations
34 consistently show that asymmetric slips occur on inward-dipping normal faults along the
35 northwest corner of the caldera. While the source mechanism from May 29 onwards is not fully
36 resolvable seismically using far-field stations, infrasound records and simulations suggest there
37 may be inflation during the collapse. The summit events are characterized by both inflation and
38 asymmetric slip, which are consistent with geodetic data. Based on the location of the slip and
39 microseismicity, the caldera may have failed in a 'see-saw' manner: small continuous slips in the
40 form of microseismicity on the southeast corner of the caldera, compensated by large slips on the
41 northwest during the large collapse events.

42

43 **Plain Language Summary**

44 Characterizing the large seismic events that occurred at the Kīlauea summit is important to
45 understand the subsurface deformation process during the 2018 eruption. There are a total of 62
46 events where the first 12 events are accompanied with long-duration seismic signals and the later
47 50 events are associated with large collapses within the caldera. There are several challenges in
48 characterizing these events due to the complex volcanic environment that can be overcome by
49 using multiple geophysical datasets including seismic waves that travel in the Earth and
50 infrasound that travels in the atmosphere to provide a more complete perspective on the seismic
51 source – its location and how it deforms. While the shallow magma reservoir at the summit
52 experiences an overall deflation throughout the eruption, we found that the reservoir inflates
53 temporarily during the earlier seismic events. For the later collapse events, the caldera slipped
54 on only one side instead of a complete subsidence of the entire caldera which is commonly
55 assumed. Our finding of both inflation and one-sided slip is consistent with other independent
56 studies and suggests this asymmetric slip may be a common feature for basaltic volcanoes like
57 Kīlauea.

58

59 **1 Introduction**

60 The 2018 Kīlauea eruption completely transformed the Kīlauea summit from its previous state of
61 small-scale continuous eruptions, starting from the drainage of the lava lake at the vent within
62 the Halema‘uma‘u crater to the eventual large-scale caldera collapse (Neal et al. 2019). During
63 the 2018 eruption, 62 large seismic events were recorded at the Kīlauea summit: the initial 12
64 events from May 17 to May 26 had moment magnitudes (M_w) between 4.3 and 4.7, and were
65 often accompanied by long-duration seismic signals; the remaining 50 events from May 29 to
66 August 2 were stronger (average M_w 5.3) and associated with broad scale collapses (Neal et al.,
67 2019). These seismic events were potentially related to a dynamic, transient process at the
68 subsurface reservoir. The presence of a shallow reservoir was well-established through modeling
69 the eruption behavior at the summit prior to 2018 including the fluctuations of the lava lake
70 level, several Very-Long-Period (VLP) seismic events, and deflation-inflation episodes.

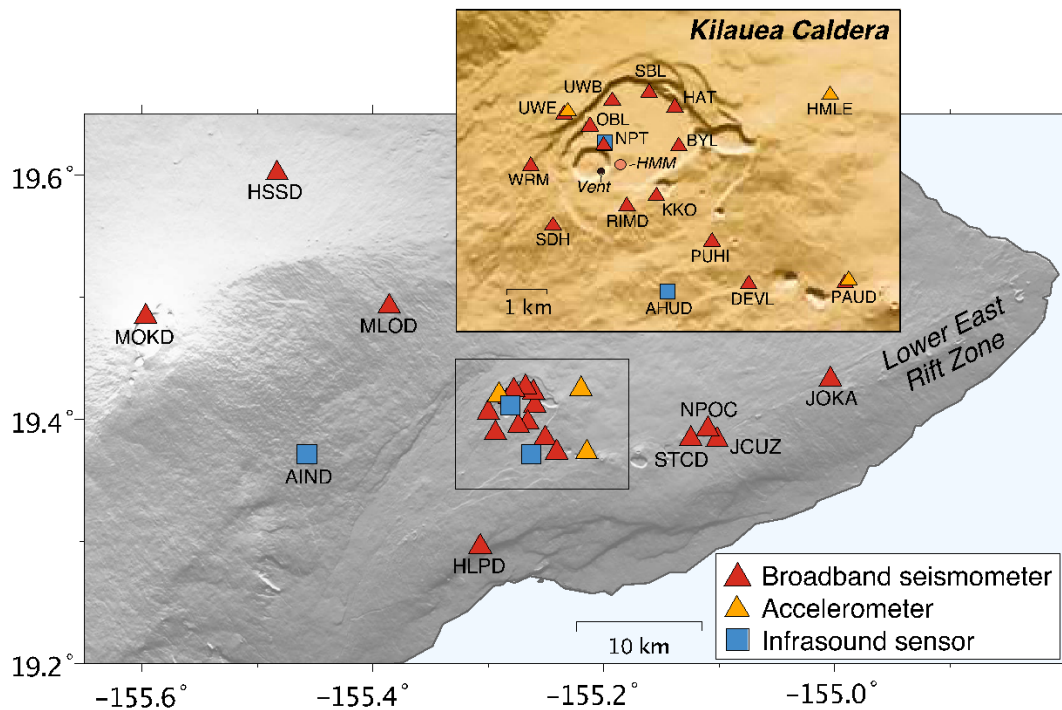
71 Analyses based on these observations including tilt inversion (Anderson et al., 2015), geodetic
72 modeling using interferometric synthetic aperture radar (InSAR) data (Baker and Amelung,
73 2012), seismic modeling of the VLP events (Dawson et al., 2010; Chouet et al., 2010), and
74 modeling of the lava-lake sloshing mode during the VLP events (Dawson and Chouet, 2014;
75 Liang et al., 2020) pointed to a reservoir slightly east of the Halema‘uma‘u crater at a depth of
76 between 1 - 2 km below the surface. The Halema‘uma‘u reservoir is thought to be hydraulically
77 connected to the vent and the lava lake (Patrick et al., 2015), a deeper magma reservoir (Poland
78 et al., 2014) and to the rift zone downstream (Anderson et al., 2015; Patrick et al., 2019). The
79 geometry of the Halema‘uma‘u reservoir is modelled geodetically as a Mogi-type spherical
80 source (Baker and Amelung, 2012) and an ellipsoidal chamber (Anderson et al., 2019), and
81 seismically as an intersecting dual-dike system (Chouet et al., 2010).

82 Characterizing the seismic events in the 2018 eruption can help us to infer the deformation
83 process beneath the summit and its relation to the overall eruption sequence. However,
84 describing complex seismic source processes at volcanic regions is challenging due to
85 observational limitations. Many caldera collapses at remote locations are monitored by seismic
86 stations at teleseismic distances as in-situ stations are rare. As a result, seismic source studies are
87 restricted to only using long-period surface wave data recorded in the far-field which have
88 several disadvantages. First, long-period waves have little sensitivity to the focal depth for
89 shallow sources. Given magma reservoirs can occupy a wide range of depths (1- 20 km),
90 accurate determination of source depths can help pinpoint the deforming reservoir. Furthermore,
91 due to zero traction at the free surface, long-period seismic waveforms related to dip-slip
92 components are weakly excited for shallow seismic sources (Julian et al., 1998). Caldera collapse
93 often generates shallow seismic sources with significant non double-couple contributions, i.e.
94 volumetric and vertical compensated-linear-vector-dipole (CLVD), which are highly correlated
95 (Kawakatsu, 1996). The correlated waveforms make it hard to distinguish source processes such
96 as reservoir pressurization, crack opening or closing, or shear slip around a ring fault (Fukao et
97 al., 2018; Sandanbata et al., 2021). The combined issues of indeterminate focal depth and weak
98 excitation for shallow source can be overcome using higher frequency waves up to 0.15 Hz;
99 However, the trade-off issue between the volumetric component and vertical CLVD still remains
100 (Hejrani and Tkalčić, 2020). Characterization of non double-couple sources can be improved by
101 increasing the coverage of the source focal sphere. An example is the analysis of the volcanic
102 earthquake at the submarine Smith Caldera near the Izu-Bonin Arc in the western Pacific. The
103 pressure gauge array which samples the upper hemisphere of the source radiation pattern,

104 recorded a strong tsunami motion, meaning the caldera seafloor is uplifted and this process could
 105 not be uniquely determined from seismic data alone (Fukao et al, 2018).

106 The 2018 Kīlauea summit eruption were recorded by several types of geophysical instruments at
 107 the summit and southern part of the island including broadband seismometers, accelerometers,
 108 and infrasound arrays (Figure 1), providing a unique opportunity to characterize the seismic
 109 sources and infer the underlying deformation process. In this study, we employed multiple
 110 techniques including particle motion analysis, seismic moment tensor analysis, infrasound travel
 111 time study, and infrasound simulations. Seismic moment tensor analysis using long period waves
 112 provides a first-order constraint on the seismic source representation. We showed that near-field
 113 summit stations are essential to resolve the volumetric contribution. Using regional data of
 114 relatively high frequency waves also allows for stable inversions of the faulting mechanism.
 115 Infrasound and particle motion analyses further provide the crucial constraints on source depth
 116 and location which is hard to resolve from seismic source inversions alone. Finally, we
 117 confirmed our results with an independent teleseismic moment tensor inversion, compared our
 118 results to geodetic analysis, and described the chronology of the Kīlauea summit deformation.

119



120

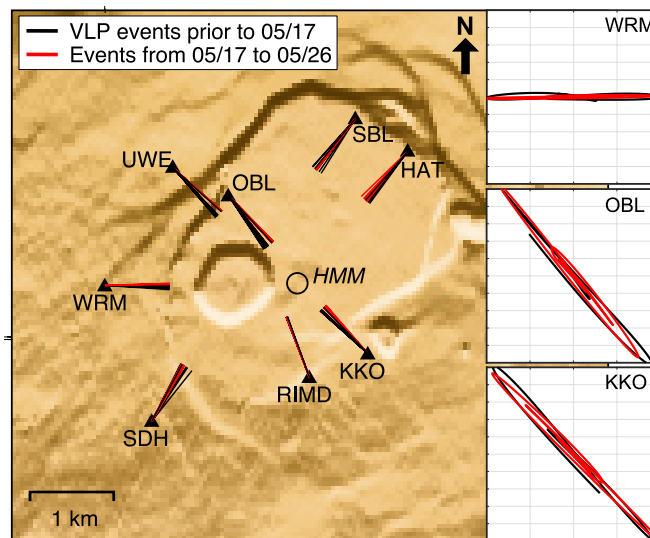
121 **Figure 1.** Map of Kīlauea Caldera and Lower East Rift Zone before the 2018 eruption. The inset
 122 focuses on the summit including the smaller Halema'uma'u crater (dashed line), the vent with an
 123 active lava lake (black dot) and the predicted centroid location of the Halema'uma'u (HMM)
 124 magma reservoir (orange circle). The map also shows the regional geophysical instruments
 125 maintained by USGS Hawai'i Volcano Observatory (HVO): broadband seismometers in red
 126 triangles, accelerometers in yellow triangles, and infrasound sensors in blue squares.

127

128 2 Event location from particle motion analysis

129 Particle motion provides an independent constraint to locate the source and track how a seismic
 130 source migrates, which is challenging in seismic moment tensor inversions due to reduced
 131 sensitivity to location at long periods. Previous work by Kawakatsu et al. (2000) at Aso volcano
 132 found that near field static displacements of large seismic events show a rectilinear polarization
 133 pointing towards the source location. To measure the particle motions, we applied a long period
 134 filter (20 – 50 seconds) to the seismic waveforms and measured the back-azimuth by treating the
 135 two horizontal components as a covariance matrix and calculating the angle of rotation of the
 136 eigenvector with the largest eigenvalue. Strong velocity heterogeneities and sharp topographic
 137 change can distort the ray path from the direct great-circle path, causing the particle motions to
 138 not project onto a common point. Liang and Dunham (2020) have shown that the seismic signals
 139 from the past VLP events shortly before the first large explosive events originate from the known
 140 Halema‘uma‘u (HMM) reservoir. Therefore, we compare the particle motion of individual
 141 stations measured from the seismic events during the eruption and these VLP events to identify if
 142 the source is the same. We found that the horizontal particle motions for the first 12 events (May
 143 17 to May 26) overlap with the particle motions from the past VLP events, indicating an
 144 identical seismic source localized at the HMM reservoir (Figure 2). The analysis using the radial
 145 and vertical particle motions also showed minimal difference in the dip angle (Figure S1),
 146 meaning the events have a common source depth, determined to be at 1 km by Liang and
 147 Dunham (2020).

148

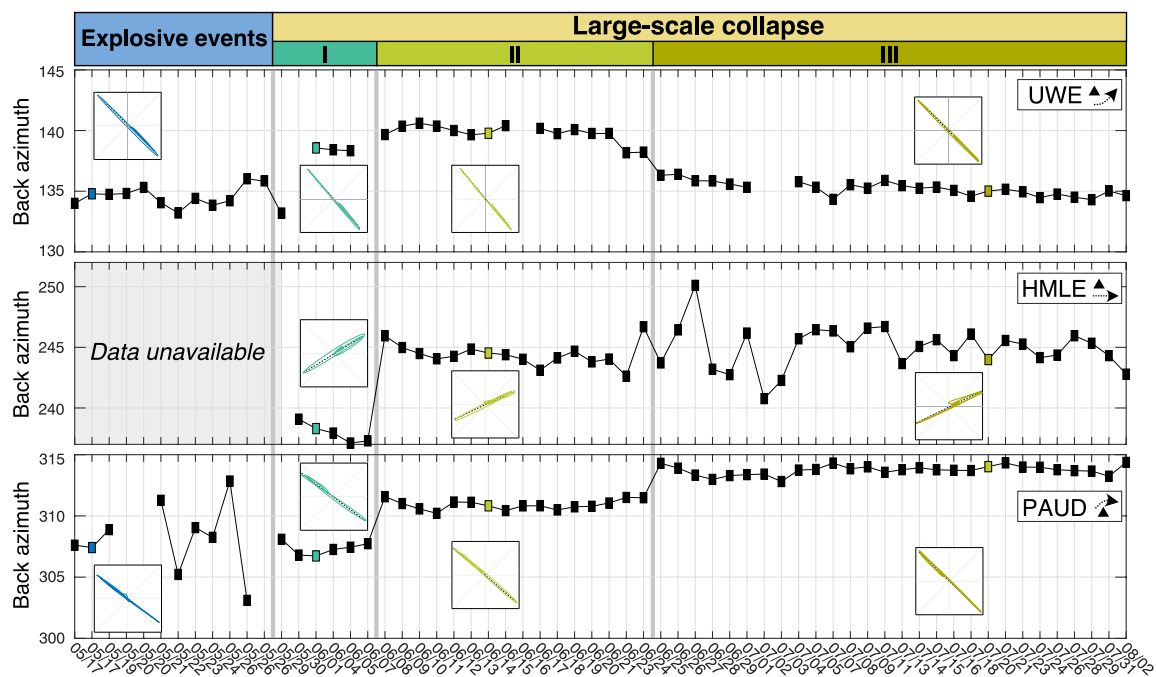


149

150 **Figure 2.** Back azimuths of horizontal particle motions recorded by broadband seismometers on
 151 the summit for the Very Long Period (VLP) events prior to May 17 (i.e., March 15, April 6, May
 152 9 and events studied by Liang et al. (2019) between May 3 and May 7) and the first twelve
 153 explosive seismic events (May 17 to May 26 in red). Right plots show the comparison of particle
 154 motions from a VLP event to an explosive event recorded at station WRM, OBL and KKO.

155 We further analyzed the horizontal particle motion of the accelerometer recordings (UWE,
 156 HMLE, and PAUD) which remained unclipped throughout the eruption. The particle motions are

157 measured using waveforms deconvolved to velocity and filtered at 0.03 to 0.08 Hz. The particle
 158 motion showed four distinct episodes (Figure 3). For the first 12 events, the accelerometer
 159 closest to the caldera, UWE, showed a consistent back-azimuth, indicating a localized source.
 160 For the remaining 50 events, we see a small (less than 5 degree) but systematic change in back-
 161 azimuth at station UWE and PAUD with a marked transition around June 7-8 and June 24-25.
 162 The decrease in back-azimuth for UWE which is located northwest of the caldera, and the
 163 increase in back-azimuth for PAUD, which is southeast of the caldera, suggest that the seismic
 164 source is migrating eastward. Given HMLE is located to the east of caldera, we expect minimal
 165 changes in the back-azimuth from an eastward migration of the source. The timing of the
 166 transition determined by the particle motion corroborates with the changes in displacement
 167 behavior observed by several global position system (GPS) stations at the caldera (Tepp et al.,
 168 2020).



169

170 **Figure 3.** Back azimuths of horizontal particle motions recorded at three accelerometers (UWE,
 171 HMLE and PAUD) for all large seismic events from May 17 to August 2. A selection of particle
 172 motions for some events, which are color-coded, are plotted and the measured back azimuths are
 173 marked in thick dashed line. The arrows in the top right insets show the direction of the source
 174 migration with respect to the station location. Unreliable measurements are discarded. The
 175 quality of the particle motion measurement is shown in Figure S2.

176 3 Moment tensor analysis using summit and regional stations

177 3.1 Methodology

178 Seismic-source tensors provide important information about the deformation process including
 179 event size, pressurization, and fault geometry. By decomposing the source tensor (e.g., Chapman
 180 and Leaney, 2012), we can determine the relative contribution of the isotropic term, which
 181 represents pressure change, and the deviatoric term which describes the displacement

182 discontinuity on a fault and can be further decomposed into double-couple (DC) and CLVD
183 components. In this study, we used the generalized Cut-and-Paste (gCAP) moment-tensor
184 inversion method (Zhao and Helmberger, 1994; Zhu and Helmberger, 1996; Zhu and Ben-Zion,
185 2013) which allows independent time shifts for all three components while cross-correlating the
186 predicted and observed waveforms to minimize the errors due to inaccurate event location and
187 velocity model. The time-shift window is carefully selected to avoid cycle-skipping. The Green's
188 functions are computed with the frequency-wavenumber method described in Zhu and Rivera
189 (2002) using a 1-D velocity model constructed from a layer average of the 3-D local P-wave
190 seismic tomography (Lin et al., 2014). We approximate the source time function with an
191 isosceles triangle and determine the duration through grid search between 1 and 25 seconds.

192 We used a selection of broadband seismometers maintained by the USGS Hawaiian Volcano
193 Observatory, 14 near-field stations within 3 km radius from the summit and 8 regional stations
194 within 35 km radius (Figure 1). The near-field summit stations, which are directly above the
195 source and sensitive to the upper hemisphere of the source radiation pattern, are crucial to
196 determine the isotropic component of the moment tensor as the isotropic and vertical-CLVD
197 terms produce similar azimuthal radiation patterns in the far-field. To illustrate, the synthetics
198 from the GCMT solution, which has a strong vertical-P CLVD component, and the best
199 deviatoric solution determined by gCAP fit the regional data and not the near-field data recorded
200 at the summit (Figure S3 and S4). Full moment tensor solution that searches for all DC, CLVD
201 and isotropic terms can fit the near-field data well for all azimuths (Figure 4a). However, these
202 near-field data are only available for the initial 12 events and are clipped for the remaining 50
203 events. Hence, we performed separate inversions for the early (Section 3.2) and later events
204 (Section 3.3).

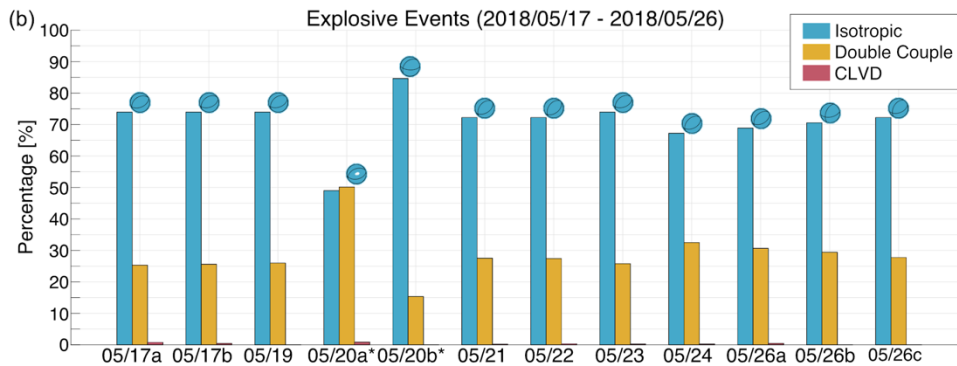
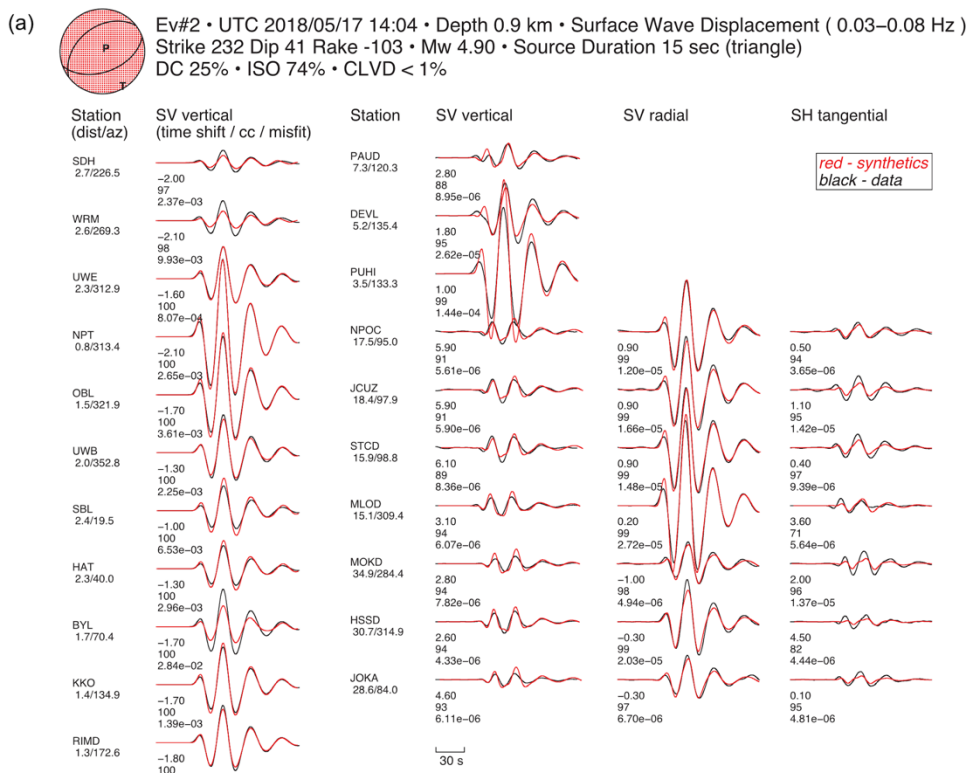
205 Stations further away on the island are not used as they do not show clear single elliptical-
206 particle motions owing to a strong multipathing behavior, indicating surface waves arriving at
207 multiple azimuths. Summit stations are limited to the vertical component as the horizontal
208 components at long period are highly susceptible to tilt due to deflation or inflation processes
209 (Wielandt and Forbriger, 1999). Waveforms recorded at near field (< 3 km) are weighted less
210 than the regional data to prevent their large amplitude from dominating the inversion results.
211 Based on the particle-motion results, the source is set at the HMM reservoir (19.4069° , -
212 155.2752° ; from Baker and Amelung, 2012), which is similar to centroid location determined by
213 Liang and Dunham (2020). The inversion is repeated for a range of source depths between 0.1
214 and 5 km.

215 3.2 Early explosive events (05/17 – 05/26)

216 The full moment tensor inversion results show that for the first 12 events, the best-fit solutions
217 have moment magnitudes between M_w 4.37 to 4.95 with high isotropic contribution (average
218 72.4%), significant DC (average 27.4%), and negligible CLVD ($< 1\%$) (Figure 4b). The strike,
219 rake, and dip of the focal mechanisms are also similar throughout the events (average 66/-72/49)
220 and are stable as supported by the bootstrapping analysis (Figure S5). Grid search results show
221 that most of the early events fit well at a depth range between 0.7 and 2.0 km, with the best depth
222 at 900 m from the surface (Figure S6). The depth, with the uncertainty, is similar to the depths
223 estimated for HMM reservoir from seismic studies at ~ 1 km (Chouet et al., 2010; Liang and
224 Dunham, 2020) and from geodetic inversions at ~ 2 km (Baker and Amelung, 2012; Anderson et
225 al., 2019).

226 The source durations of these events range between 10 to 20 seconds which are an order of
 227 magnitude longer than the durations for similar-magnitude tectonic earthquakes (Kanamori and
 228 Brodsky, 2004). The source durations correlate well with the length of the long-period pulse in
 229 the raw waveforms (Figure S7) and have no obvious correlation with other parameters such as
 230 event magnitude or event time. These long source durations are also consistent with the findings
 231 by Flinders et al. (2020) using synthetic measurements derived from GPS where the durations
 232 are best described by 26 ± 5 seconds long radially outward and upward displacement ramp
 233 function. Events 4 and 5 have exceptionally long source durations exceeding the period
 234 bandwidth of the input waveforms hence their moment tensor solutions are unreliable. An
 235 inspection on the broadband data also showed the two events are fairly complicated and appear
 236 to have multiple short and distinct subevents, unlike the other events. The use of time shifts in
 237 the gCAP inversion prevents us from determining the centroid time of the events.

238



239

240 **Figure 4. (a)** Plot of the best-fitting full moment tensor solution inverted for explosive event 2,
 241 which is highly isotropic (74%) with the strike, dip and rake value of 232, 41 and -103
 242 respectively. The waveforms are surface wave displacement filtered at 0.03 – 0.08 Hz. The
 243 observed displacements are plotted in black and the synthetics in red. The distances measured in
 244 kilometers and azimuth of the stations to the epicenter, and the time shifts used in gCAP,
 245 correlation coefficient (cc) and waveform misfit are also listed. Note that the bandpass filter
 246 applied will introduce Gibbs-ringing (as detailed in Flinders et al., 2020) to the waveforms (both
 247 data and synthetics) but does not affect the moment tensor solution. **(b)** Graph shows the
 248 similarity of the best-fitting full moment tensor solutions, focal mechanisms, and the
 249 contributions of the isotropic, CLVD, and double-couple components for the 12 explosive events
 250 between May 17 and May 26. The moment tensor solutions for events 4 and 5 (May 20a and
 251 May 20b), marked with asterisks, are poorly determined due to the anomalously long source
 252 duration.

253

254 3.3 Late collapse events (05/29 – 08/02)

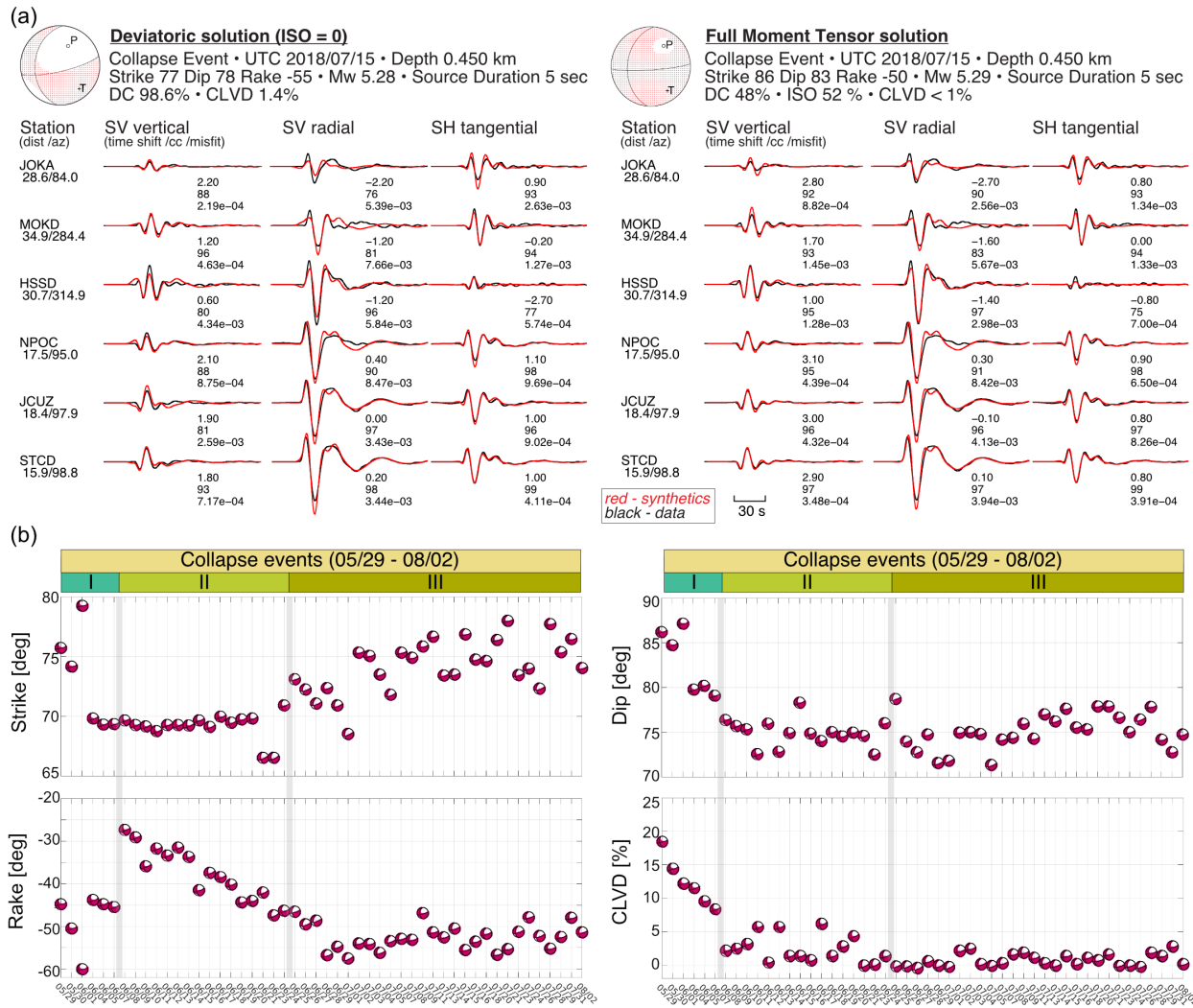
255 For the later events, the isotropic contribution cannot be determined due to the fits of deviatoric
 256 and full moment tensor solutions to the waveforms being similarly good (Figure 5a). Hence, we
 257 focused on the deviatoric solution to resolve the fault geometry (strike, rake, dip) and the
 258 strength of CLVD term. The input waveforms are filtered between 12.5 to 50 seconds (0.02-0.08
 259 Hz). The hypocenter is fixed at the HMM reservoir location as the regional waveforms are
 260 insensitive to the small changes in location around the caldera. The source depth is fixed at 450
 261 m, informed by infrasound simulations (details in Section 4.2). The preferred source duration is 5
 262 seconds based on grid search results. Bootstrapping analysis showed that there is a tight
 263 constraint on the focal mechanism despite the small number of stations (Figure S8).

264 The inversion results show that the remaining 50 events are shear slips along inward-dipping
 265 normal faults with minimal CLVD component (< 5%) (Figure 5b). The events evolve throughout
 266 the eruption with three marked transitions in the focal mechanisms. Between May 29 to June 7,
 267 the events have a relatively high CLVD term (maximum 20 %) with an average strike/rake/dip of
 268 73/-50/75. From June 8, the strength of CLVD term decreases, along with changes in the strike,
 269 rake, and dip to a new average of 69/-38/75 until June 25 when the focal mechanism stabilized
 270 and remained fairly constant until the end of the collapse sequence. The later focal mechanisms
 271 have a small CLVD component, and an average strike, rake, and dip of 74/-52/75., The
 272 transitions coincide with the changes in particle motion determined from accelerometers which
 273 show the source migrated eastward over time (Figure 3). The nodal plane is selected to be
 274 striking northeast-southwest in order to be consistent with the increasing strike value and the
 275 eastward source migration along the caldera. The inversion results suggest the roof block above
 276 the caldera has collapsed asymmetrically at its northwest corner, instead of a commonly assumed
 277 complete ring-fault slip. There may be a significant volumetric component associated with these
 278 events as observed in the rapid inflationary steps in tilt data (Anderson et al., 2019; Segall et al.,
 279 2019), but is not resolved for these events.

280

281

282



283

284 **Figure 5. (a)** Figure shows both best fitting deviatoric (left) and full moment tensor (right)
 285 solutions for collapse event 51 (July 15, 2018) can fit the regional waveforms well. The observed
 286 displacements are plotted in black and the synthetics in red. The distance and azimuth of the
 287 stations to the epicenter, and the time shift used in gCAP, correlation coefficient (cc) and
 288 waveform misfit are listed. **(b)** Figure shows the best-fitting deviatoric solutions for all 50
 289 collapse events between May 29 to August 2. The changes in strike, rake, dip, and CLVD
 290 component follow closely the transitions (marked by grey lines) observed in the particle motion
 291 measurements (Figure 3).

292

293 4 Source depth from infrasound analysis

294 Infrasound are pressure waves with frequencies below 20 Hz that can be generated during a plume
 295 eruption into the atmosphere or by shallow seismic source which its seismic energy couples with
 296 the free surface and propagates in the air at acoustic sound velocities (Fee and Matoza, 2013). As
 297 infrasound is sensitive to upward radiating energy like the near-field summit stations, it can
 298 provide additional constraint on the source processes (e.g., Fukao et al. 2018). During the 2018
 299 eruption, the nearby AHUD infrasound array recorded a variation in infrasound arrival-time and

300 waveform shape (Figure S9). For each event, we can compute the theoretical arrival time based on
301 the sound velocity and the distance from the vent to the sensor. For the first 12 events, AHUD
302 records fairly weak pressure signals, with occasional strong-upward pulses that are significantly
303 delayed from their expected acoustic arrival times. These upward pulses are also observed during
304 the VLP events prior to the large seismic events on March 15, April 6 and May 9. For the remaining
305 50 events, there are two distinct arrivals: (1) weak high frequency waves traveling at seismic
306 Rayleigh-wave velocity and (2) a strong low frequency pulse with initial downward polarity
307 traveling at acoustic speed.

308 4.1 Infrasond observations for early events

309 The arrival time of the compressional peaks are clearly observed by infrasond sensors at multiple
310 distances (< 1 km, 4.5 km and 19 km; Figure 6a). The origin time is assumed to be the catalog
311 origin time for the events during the eruption and the seismic arrival time at the closest seismic
312 station (NPT; < 1 km) for the previous VLP events. The waveforms are plotted at reduced time,
313 which is the total time subtracted by the travel time from the vent to the sensor. On March 15 and
314 April 6, we observed that the strong infrasond peak arrived at about the zero mark which is the
315 expected acoustic arrival time. From May 9 to May 26, the arrival of the infrasond peak is
316 progressively delayed in time. The time delay observed has some similarities to that at Miyake-
317 jima (Kobayashi et al., 2005) where the signal traveled along a conduit at a distinct velocity before
318 propagating as an infrasond pulse at acoustic speed from the vent to the sensor. While the signal
319 is interpreted as acoustic signal at Miyake-jima, given the large time delay (up to 33 seconds), it
320 is unlikely that the infrasond pulses are direct pressure waves from the seismic source as the
321 expected maximum time delay of these waves propagating up a hot conduit is around 3 to 5
322 seconds (~400 m/s (Morrissey and Chouet, 2001) at 1 – 2 km conduit). Simulation results also
323 suggest the infrasond pulses from the inflation at depth are weak (details in Section 4.2).

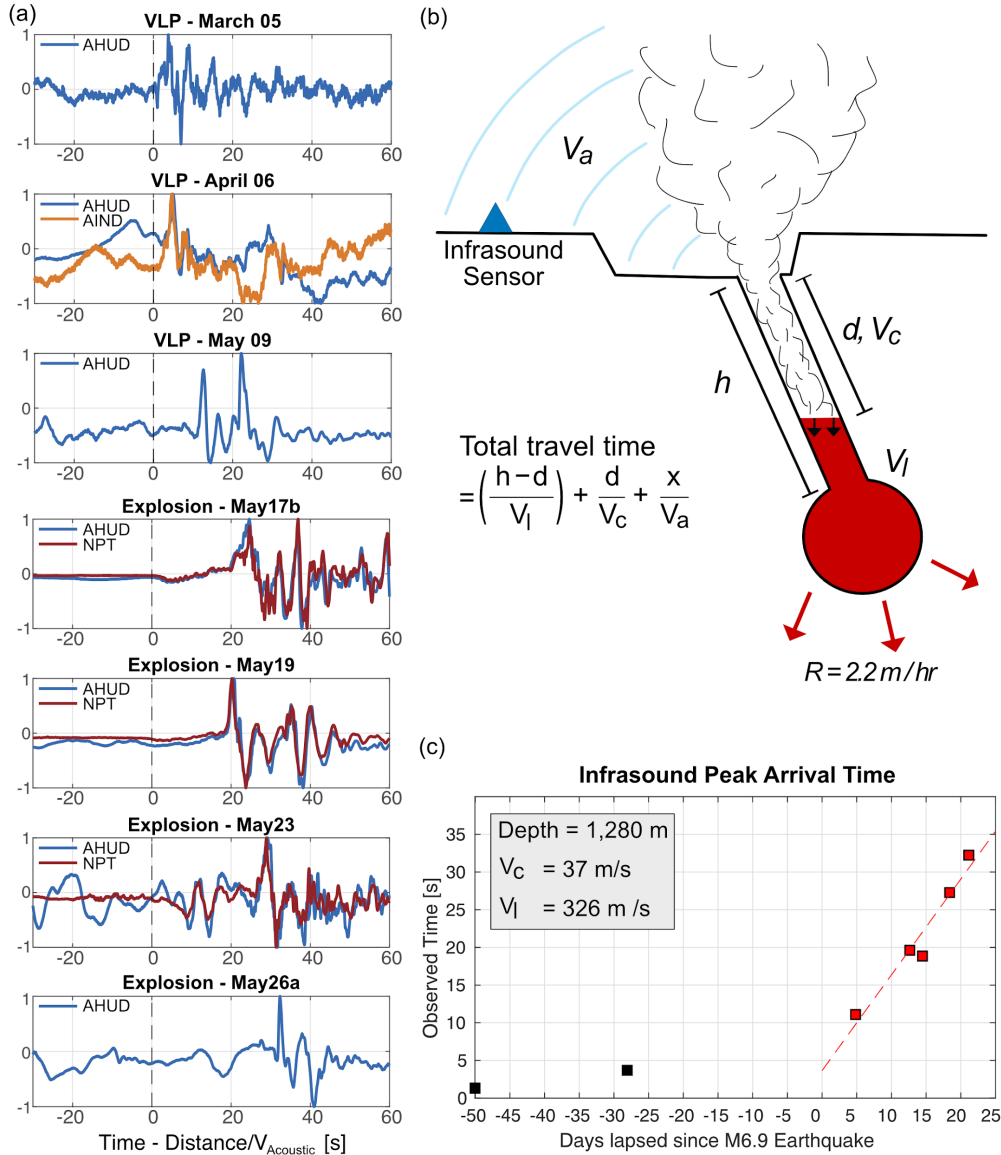
324 We hypothesize the infrasond pulse is to be a result of gas emission during the seismic event. Gas
325 emission at volcanoes has been correlated to compressional acoustic pulse (Johnson and Lees,
326 2000). The gas emission initiates at the reservoir depth, rises upward through a connected path and
327 exits at the vent. The path could be a collection of dikes but is modelled here as a simple conduit
328 as we lack details on the dike formations. The gas expansion at the vent creates an upward
329 compressional pulse and the time delay is governed by the speed of gas rising the conduit. The
330 propagation time in the conduit is controlled by the lava lake elevation, which was visible at the
331 vent throughout the spring of 2018 and started draining at an estimated rate of 2.2 meter per hour
332 on May 2 (Anderson et al., 2019). Theoretically, when the conduit was completely filled, the signal
333 arrived at the sensor at a time corresponding to the vent-to-sensor distance. As the lava lake began
334 to drain, the length of drained conduit increased, delaying the infrasond pulse. Towards the end
335 of the first 12 events, the lava level is assumed to reach the reservoir depth and the entire conduit
336 was drained. Factors like clear or clogged path and amount of gas accumulation can affect the
337 effectiveness of gas expelling from depth. These factors may explain the varying infrasond pulse
338 amplitude where pulses from the earlier events are more impulsive as the path is less drained and
339 hence potentially less clogged.

340 4.2 Source depth constrained from infrasond

341 From the infrasond arrival-time measurements, we constrain the velocity of the gas rising, the
342 speed of degassing signal in the lava medium and most importantly the length of the conduit. The

343 relation between the arrival time of the infrasound pulse and the propagation distance is described
 344 as total time, $t_{total} = (1/V_c)d + (1/V_l)(h - d) + (1/V_a)x$, where h is the length of conduit, d is the
 345 length of the drained conduit, x is the distance from the vent to the sensor, V_c is the velocity of the
 346 gas rising, V_l is the compressional velocity of the magma, and V_a is the acoustic speed at surface
 347 (Figure 6b). The term $(1/V_a)x$ is known and V_a is determined from the average slowness of the
 348 pulse crossing the AHUD infrasound array, at 340 m/s. Assuming the draining rate, R , remains
 349 constant over the course of the eruption, d is calculated by taking $d = R\Delta T$, where ΔT is the time
 350 elapsed between each eruption. To estimate h , V_c , and V_l , an additional condition is needed. Based
 351 on the hypothesis, an appropriate condition is that the entire length of the conduit is completely
 352 drained by event 12, that is $t_{last} = (1/V_c)h$. Event 12 had a very weak infrasound pulse, so we take
 353 the clear signal from a slightly earlier event on the same day (Event 10) as an approximation. With
 354 this condition and the infrasound time measurements, we obtained the values of V_c , V_l and h from
 355 a simple linear regression of the total time, t_{total} and time elapsed, ΔT . The uncertainties given in
 356 parentheses are obtained based on 95% prediction interval of the slope. We estimated h to be 1280
 357 (851 – 1778) m, V_c to be 37 (26 – 55) m/s, and V_l to be 326 (137 – 1702) m/s (Figure 6c). The
 358 estimated h is slightly deeper than the depth of the seismic source obtained from the seismic
 359 moment tensor inversion at 900 m, but still within the uncertainty from inversion (0.7 to 2 km).
 360 The estimated h is also consistent with the lava lake elevation at the end of the explosive events at
 361 1260 m, which is estimated from the draining rate (Figure S10). The value of V_c is in the same
 362 order of magnitude as strong Strombolian-type degassing (31 – 34 m/s in Patrick et al. (2007); 38
 363 – 53 m/s in Taddeucci et al. (2012)) and is comparable to the previously recorded plume velocities
 364 at Kīlauea (ranging between 5.8 and 16.6 m/s in Fee et al. (2010)). The value of V_l in the order of
 365 ~ 100 s to ~ 1000 s m/s suggests that it is not the velocity of fragmentation wave in the magma (which
 366 is in the order of ~ 10 s m/s, e.g., Alidibirov, 1994; Spieler et al., 2004) but more likely the
 367 compressional velocity of magma with some fraction of bubbles (in the order of ~ 100 s m/s, e.g.,
 368 Kumagai and Chouet, 2000). However, we will not overly interpret V_l as the uncertainty of V_l is
 369 large. Given V_l is at least an order of magnitude larger than V_c , the infrasound time delay is
 370 governed by the inverse of rising gas speed, V_c .

371



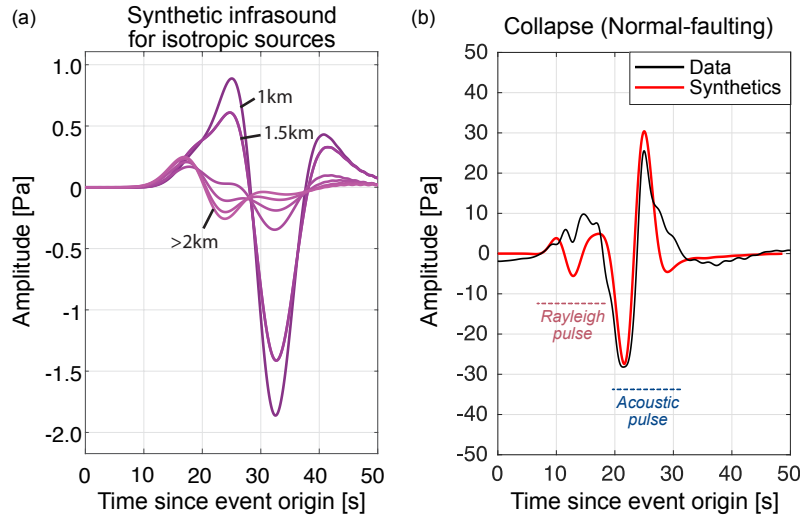
372

373 **Figure 6. (a)** Plot shows the raw infrasound data for three VLP events and four selected
 374 explosive events. The data are plotted in normalized amplitude at reduced velocity, corrected for
 375 the travel time from the vent to the sensor. **(b)** Schematic shows the variables involved in
 376 calculating h , i.e. length of the conduit, which include: d , the length of the drained conduit; x , the
 377 distance from the vent to the sensor; V_c , the velocity of the rising plume; V_i , the compressional
 378 speed of the magma; and V_a , the acoustic speed at surface. The lava lake is draining at an
 379 estimated speed of R (2.2 m/hr from Anderson et al., 2019). **(c)** Graph shows the observed time
 380 delay in the peak arrival against the number of days elapsed since the M6.9 earthquake The
 381 estimated values of h , V_c and V_i are obtained from linear regression using the events marked in
 382 red.

383 4.3 Infrasound simulation for explosive and collapse events

384 We also tested the infrasound data against the seismic moment tensor solutions. To simulate, we
 385 used a hybrid Galerkin – 2D spectral element method (Brissaud et al., 2017) which accounts for

386 the elastic wave propagating away from the seismic source and the acoustic wave generated due
 387 to the coupling between solid Earth and atmosphere. The effects of atmospheric structure and
 388 variability can be ignored for short distance simulation (4.5 km). Simulation using the highly
 389 isotropic solution from the earlier events generates synthetics which have very weak amplitudes
 390 and arrive at the expected acoustic travel times (Figure 7a), supporting the previous hypothesis
 391 that the observed late strong upward pulse does not originate from seismic source. For the later
 392 collapse events, infrasound simulations using the deviatoric moment tensor solution are able to
 393 reproduce the seismic-acoustic coupling of both the early, high frequency Rayleigh pulse and the
 394 late, low frequency, high amplitude acoustic pulse (Figure 7b).



395

396 **Figure 7. (a)** Plot shows the comparison of synthetic infrasound generated at different source
 397 depths using the moment tensor solution from Event 2 which is highly isotropic. **(b)** Plot shows
 398 the comparison of observed infrasound (black) with synthetics (red) from the predominantly
 399 normal faulting moment tensor. The synthetic fits the early Rayleigh pulse and the downward
 400 acoustic pulse but does not fit the late broad peak at 25 seconds. Both data and synthetics are
 401 filtered with a second-order Butterworth filter from 0.04 to 0.5 Hz.

402

403

404 We prefer to use the amplitude ratio between the acoustic and Rayleigh pulses rather than the
 405 absolute amplitude. There are a few factors which makes modeling the absolute amplitude
 406 challenging: the primary one being the near-surface velocity model which is not easy to
 407 characterize but can greatly amplify the acoustic pulse (Martire et al., 2018). Using the amplitude
 408 ratio can mitigate some of the potential biases in the choice of velocity model and 2d modelling
 409 assumptions. For comparison, we scaled the synthetics to match the amplitude of the observed
 410 downward acoustic pulse. The amplitude ratio is highly dependent to the source depth. For a
 411 shallow source, the acoustic pulse is amplified compared to the Rayleigh pulse (Figure S11),
 412 which is consistent with the infrasound observations for underground nuclear explosions
 413 (Averbuch, 2020). For source depths shallower than 1 km, the amplitude ratio is large due to
 414 stronger Rayleigh pulse; for deeper source depths, the amplitudes for both pulses are similarly

415 weak. Other factors such as a slow layer near the surface do not affect deeper sources and can
416 further increase the amplitude ratio for shallow sources (Figure S11).

417 Webcam recordings (from HVO) and geodetic measurements (Segall et al., 2020) suggest there
418 is roof subsidence during each collapse events, which is reinforced by the similarity of the
419 infrasound observations at Kīlauea and at Miyake-jima in which Fujiwara et al. (2014) explained
420 the observation at Miyake-jima with partial roof subsidence. While surface subsidence can
421 generate infrasound signal, we recognize the subsidence is caused by the normal-faulting event,
422 and by simulating the earthquake source directly, we can model the infrasound signal and use it
423 to provide constraints on the seismic source depths which is important for the moment tensor
424 analysis. Based on qualitative comparison with the observed amplitude ratio, we estimate that the
425 seismic source of the collapse events should be at depths shallower than 1 km. For seismic
426 magnitude of Mw 5.0, the rupture length is close to 1 km (Kanamori and Anderson, 1975).
427 Hence, we set the source centroid depth at 450 m for the moment tensor analysis (Section 3.3) to
428 mimic fault rupturing all the way to the surface.

429 The infrasound data has a late strong peak arriving at 25 seconds which is broader than the initial
430 downward pulse (Figure 7). The normal faulting solution, however, cannot fully fit the observed
431 signal and only produces synthetics with peak equal or weaker amplitude and symmetric in pulse
432 width compared to the downward pulse, regardless the source depths and near-surface source
433 model. This mismatch in amplitude and duration may potentially be accounted for by isotropic
434 sources at 1 – 1.5 km depth, which has a weak peak arriving at the right time range, and points to
435 a potential dual process of normal-faulting and inflation during the collapse event. While the
436 topography is not expected to play a significant role for low-frequency acoustic waves, a detailed
437 analysis which considers other important factors such as the interplay between the choice of
438 source time function and velocity model is needed to accurately reproduce the absolute
439 amplitude and is beyond the scope of this study.

440 **5 Discussion**

441 5.1 Factors controlling isotropic component

442 Seismic moment-tensor characterization is key to identify the source mechanism during volcanic
443 eruptions (e.g., Bárðarbunga, Iceland (Gudmundsson et al., 2016; Ágústsdóttir et al., 2019),
444 Piton de la Fournaise, Réunion Island (Duputel and Rivera, 2019; Fontaine et al., 2019), Miyake-
445 jima, offshore Japan (Kumagai et al., 2001), and Kīlauea, Hawaii (Alvizuri et al., 2021; this
446 study). However, there are several factors that can affect the moment tensor, in particular the
447 resolved isotropic component. In this study, we emphasized the necessity of using near-field data
448 to constrain the isotropic component and using other independent observational data to constrain
449 depth. In Figure S12, we found that without the near-field data, the full moment tensor solutions
450 for explosive and collapse events have negative isotropic component across all depths, indicating
451 implosion which is inconsistent with the inflationary signal observed in tilt and GPS (Anderson
452 et al., 2019). The results of negative isotropic component hold regardless of the choice of
453 velocity models. This unstable inversion is due to the trade-off between the vertical-P CLVD and
454 negative isotropic components at distant stations. There is also a strong correlation between
455 depth and the strength of the isotropic component. Seismic moment tensor inversions alone have

456 limited sensitivity for depth as they give similar error misfits for a range of depth with the
 457 smallest misfit at deeper depths. Therefore, other independent data, such as particle motion and
 458 infrasound, are important to constrain depth and, in turn, the isotropic component.

459 In our moment tensor analyses, the volumetric component is represented by an isotropic inflation
 460 at a spherical source. However, the M_{xx} and M_{yy} components dominate over
 461 the M_{zz} components (see moment tensor catalog in Supporting Information), suggesting that the
 462 inflation may occur along vertical cracks, analogous to the intersecting-dike system inferred
 463 by Chouet et al. (2010). This uneven amplitude ratio between the principal moments is also
 464 observed at Miyake-jima (Kumagai et al., 2001). Note that, the true M_{zz} may be greater than
 465 measured seismically as M_{zz} is preferentially damped in seismic observations for shallow seismic
 466 sources due to zero traction at the free surface.

467 5.2 Asymmetric slip resolved from teleseismic moment tensor inversion

468 The 2018 Kīlauea caldera collapse bears much resemblance to the 2014 Bárðarbunga caldera
 469 collapse in Iceland where the seismicity focused on one corner of the caldera and at shallow
 470 depths not deeper than 4 km (Ágústsdóttir et al., 2019). The source mechanisms at Bárðarbunga
 471 were also predominantly double-couple on inward-dipping normal faults. This asymmetric slip
 472 differs from the commonly assumed piston-type collapse where the entire ring fault slips during
 473 the caldera collapse. To confirm the partial ring-fault slip, we conducted another independent
 474 moment tensor inversion for all 50 collapse events using very long period teleseismic waves
 475 (over ~ 100 s) to solve for the deviatoric solution. An advantage in using very-long period data is
 476 that complex velocity structures around the caldera will not affect the inversion results.

477
 478 Because the small contribution to very long period seismic waves by the dip-slip components in
 479 shallow sources, there are large uncertainties in estimating the dip angle and seismic moment
 480 (Sandambata et al., 2021). Hence, following the method in Sandambata et al. (2021), we
 481 constrained the ring fault geometry by focusing only on the resolvable components of the
 482 inverted moment tensor: vertical CLVD (\mathbf{M}_{vCLVD}) and strike-slip (\mathbf{M}_{SS}) components (Text S1;
 483 Figure S13). This resolvable moment tensor ($\mathbf{M}_{RES} = \mathbf{M}_{vCLVD} + \mathbf{M}_{SS}$) relates to the ring-fault
 484 geometry in two ways. Firstly, the ratio of CLVD moment to the resolvable moment (k_{CLVD})
 485 positively correlates the short arc angle or the fraction of the ring fault that slipped (Figure
 486 S13c). Secondly, the direction of the pressure (P) axes of \mathbf{M}_{SS} gives the orientation of the fault
 487 plane measured at the midpoint of the curved fault (Figure S13d). The P-axis orientation and the
 488 relationship between k_{CLVD} and the arc angle are independent of dip angle and scalar seismic
 489 moment and hence can be estimated without the dip-slip component. The procedure for the
 490 inversion is in Text S2. Note that there is a trade-off between vertical-P CLVD and pure positive
 491 isotropic sources due to the similarity in far-field waveforms (Figure S14) but we found that
 492 estimation of k_{CLVD} is only reduced even when we assume an additional pure positive isotropic
 493 component for the inversion (see Text S2). Hence, we constrained zero isotropic contribution for
 494 the inversion to estimate the upper limit of the k_{CLVD} value, enabling us to infer the maximum arc
 495 angle of the ring fault that slipped.

496
 497 The results from the moment tensor inversion using global stations for all the 50 collapse events
 498 show normal-faulting focal mechanism with consistent k_{CLVD} value and P-axis orientation
 499 (Figures S15 and S16). The k_{CLVD} value is small, indicating the ring fault has partially slipped

500 with an arc angle less than 90° . The P-axis has a strike of northeast-southwest, which suggests
501 the fault plane can be either along northwest or southeast corner of the ring fault. The teleseismic
502 moment tensor solution is consistent with the inward-dipping normal faulting solution derived
503 using regional stations and supports an asymmetric slip during the collapse events. The evolution
504 in focal-mechanism properties throughout the collapse events, as seen in the local moment tensor
505 inversion, cannot be observed at very-long periods.

506 5.3 Reconciling seismic, infrasound and geodetic observations

507 The characterization of the large seismic events at the Kīlauea summit sheds light on the
508 underlying mechanisms driving the complex sequence of early VLP-dominant events and
509 subsequent broad-scale collapse events. Several mechanisms have been proposed to explain the
510 VLP signals at the Kīlauea summit, including (1) gas slug ascending, expanding and eventual
511 bursting, exciting the VLP signal at depth (Chouet et al., 2010), and (2) rockfalls impacting the
512 lava lake, triggering both plume and VLP signal from the pressure transient transmitted along the
513 conduit (Orr et al., 2013). Early in the 2018 eruption, large ash plumes were frequently observed.
514 However, many of these plume eruptions occurred outside of the VLP-dominant events, some
515 after the events have ceased, hence the VLP seismic signal and ash plume generation may not be
516 necessarily linked. On the other hand, the consistency of the seismic source at the Halema'uma'u
517 reservoir depth, obtained through particle motion studies, seismic moment tensor inversion, and
518 infrasound analysis, suggests that the magma reservoir governs the seismic behavior. One way to
519 generate a volumetric seismic signal is by pressurizing the magma chamber through an intrusion
520 of an overburden roof or 'piston', resulting in transient expansion in reservoir, similar to the
521 mechanism suggested for Miyake-jima volcano (Kumagai et al., 2001) and for Kīlauea from
522 geodetic observations (Segall et al., 2019, 2020). Rockfall could also be a possible trigger. As the
523 conduit empties during the eruption, rockfalls may become more frequent, generating explosions
524 and degassing signals almost simultaneously. However, the seismic characters of the later
525 collapses can be explained dominantly by fault slipping, hence we suggest the early seismic
526 events are a result of fault slipping into the Halema'uma'u reservoir, driven by magma
527 withdrawal from summit.

528 Our finding is consistent with the geodetically-inferred 'slip and inflation' model by Segall et al.
529 (2019 and 2020) where during the caldera collapse, the roof block slips into the Halema'uma'u
530 reservoir, inducing a proportionate inflation within the reservoir. In particular, the GPS
531 displacement pattern imposes that the slip should occur along a steep inward-dipping normal
532 fault, which is consistent with our resolved focal mechanisms of shear slip along inward-dipping
533 normal fault with an average dip of 75° . Unlike a symmetric ring-fault slip proposed by Segall et
534 al. (2019 and 2020), two independent moment-tensor inversions show that the later collapses slip
535 partially along the northwest corner of the caldera. The partial faulting may explain the
536 asymmetry observed in GPS displacement where the geodetic model under-predicts the
537 displacements along the northwest and southeast corners; and over-predicts those on the
538 orthogonal corners.

539 With the constraints from near-field stations, particle motion and infrasound, we could conclude
540 that an extended inflation occurred at the Halema'uma'u reservoir during the earlier events, as
541 suggested by the long seismic source duration (10-20 seconds). There is also evidence for the
542 'slip' process expected from the inflation as all the early events show substantial (25%) double-
543 couple contribution with strike, rake and dip values consistent to a normal faulting behavior.

544 Based on the InSAR data, the slip may occur on a buried fault and only cause a minor surface
545 depression close to the predicted center of the Halema'uma'u reservoir (Anderson et al., 2019).

546 For the later collapses, seismic data can detect the slip process but not the corresponding
547 inflation which is inferred from the infrasound-simulation results. The particle motions from the
548 accelerometer data were also able to track the evolution of the slip which radiates most of the
549 seismic energy. However, we postulate that the slip process happens before the inflation, which
550 is consistent with the process described in 'slip and inflation' model (Segall et al., 2019 and
551 2020). Butler (2018) compiled stacked antipodal PKIKP polarities for the collapse events that
552 capture the initial seismic energy propagating vertically downward away from the collapse
553 source to the antipodal ends in southern Africa. These PKIKP phases show dilatational first
554 motions which only fit solutions with minimal isotropic component at less than 5% (Figure S17),
555 supporting an initial slip process.

556 5.4 Chronology of the Kīlauea summit deformation

557 The chronology of the summit deformation during the 2018 eruption is summarized in Figure 8.
558 The drop of lava lake elevation beginning May 2 indicates a reduction in the magma reservoir
559 pressure (Anderson et al., 2019), causing the inert fault structures within the caldera which was
560 previously supported by the reservoir pressure to fail. The slip intruded into the Halema'uma'u
561 chamber, pressurized the chamber at depth, and generated long-duration volumetric signals. The
562 slip could potentially trigger gas escaping at depth in two ways: (1) by promoting magma
563 fragmentation with the dynamic pressure perturbation or (2) via the "stomp-rocket" model
564 proposed by Shelly and Thelen (2019), in which the sudden compression due to the collapsing
565 roof block expels the accumulated gas at the top of the reservoir and generates infrasound pulse.
566 Given the low speed of magma fragmentation (in Section 4.2), the "stomp-rocket" model is most
567 probable, and it also fits our hypothesis of how the infrasound pulse is generated, which is by gas
568 rising from depth and expanding at the vent.

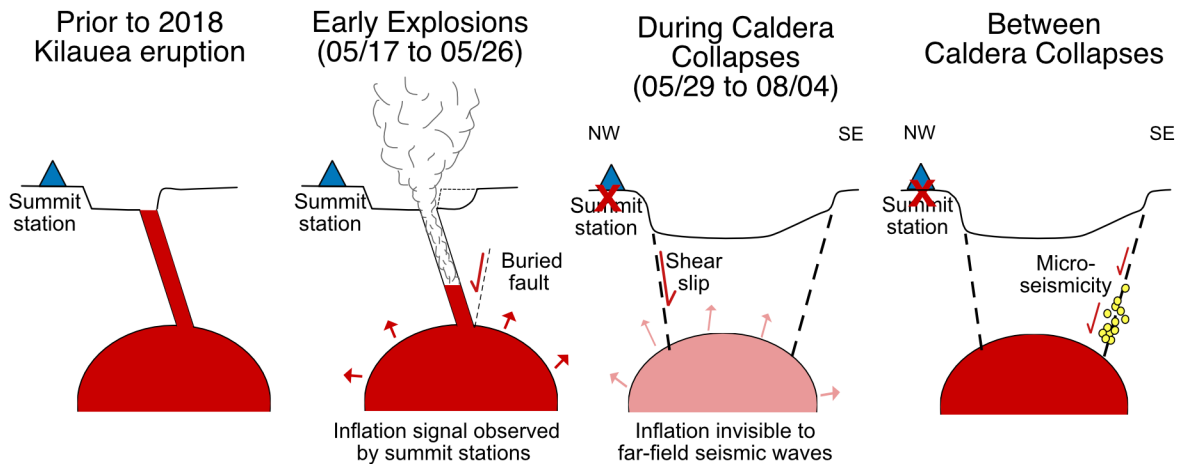
569 The transition from the early inflationary events to the later collapse events is intriguing as it
570 coincides with a coalescence of fissure eruptions at the Lower East Rift Zone to a single fissure
571 (Fissure 8) with high effusion rate (Neal et al., 2019). This high effusion rate may have
572 accelerated the decrease of magma pressure at the summit, driving a series of normal-faulting
573 collapse events. The initial collapses (May 29- June 7) have a relatively high CLVD component
574 (~12%), which is an apparent effect of slip along curved faults. The later collapses (June 8 – 24,
575 June 25 – August 2) have little CLVD component, indicating the faults are more linear. The rake
576 also becomes increasingly negative and stays constant from June 25 onwards, suggesting the
577 faulting behavior is becoming purely normal. Based on the increasing strike value and the
578 eastward source migration observed in particle motion, the slips developed over time across
579 continuous fault-like structures bounding the caldera. This fault could be the reactivation of a
580 pre-existing ring-fault, the development of a new ring-fault structure or failures along pre-
581 existing dike structures.

582 The most notable characteristic is that the caldera collapse is asymmetric, confined to the
583 northwest corner of the caldera. There are a few potential scenarios that may have encouraged
584 such asymmetry. Prior to 2018, Kīlauea summit has experienced multiple episodes of fissure
585 eruption, most recently in 1974 on the floor of Halema'uma'u crater (Holcomb, 1987) with
586 similar strikes to the ones obtained in this study. The repeating eruption may have created
587 heterogenous mechanical properties across the caldera, which fails under different stress

588 thresholds, and contribute to the observed asymmetric collapse. The asymmetry can also be
 589 formed as the summit is subjected to a prevalent extensional stress due to a seaward motion of
 590 the volcano's south flank (Poland et al., 2014), which is reflected in the similar orientation of the
 591 pressure and tension axes observed in all the seismic events. The asymmetry does not preclude
 592 an overall subsidence of the roof block as a limited number of GPS stations within the caldera
 593 measured downward vertical displacement during the collapse (Neal et al., 2019), but indicates
 594 there is a more substantial slip on the northwest side.

595 The majority of the relocated large collapse events in Shelly and Thelen (2019) occurred at the
 596 northwest corner of the caldera, consistent with our findings (Figure S18). Shelly and Thelen
 597 (2019) also relocated the microseismicity clusters in between the caldera collapses and
 598 interestingly, they show a strong asymmetry, concentrating at the eastern half of the caldera
 599 opposite of the collapse fault plane. The occurrence frequency of the microseismicity has a
 600 consistent pattern of increasing from few and peaking right before the collapse event. The final
 601 topography images show an overall subsidence of the roof block by the end of the eruption
 602 (Lundgren et al., 2019), which may give the impression that the roof block dropped in a single
 603 block during each collapse. However, given the distribution of large slip and microseismicity, it
 604 is possible that the roof piston may have failed in a 'see-saw' manner in two stages: small
 605 continuous slips in the form of microseismicity on the southeast corner of the caldera,
 606 compensated by major large slips on the northwest corner during the large seismic events.

607



608

609 **Figure 8.** Schematic shows the chronology of the Kīlauea summit deformation during the 2018
 610 Kīlauea eruption: (1) Prior to the eruption, the lava-lake level reached the vent and started to
 611 decrease on May 2. (2) The early seismic events show strong inflation signal observed by
 612 summit stations and are accompanied by occasional plume eruptions. Shear slip occurring on
 613 buried fault may cause a minor surface depression. (3) The asymmetric collapses are
 614 characterized as normal faulting along inward dipping fault on the northwest corner of the

615 caldera. Inflations cannot be resolved without the summit stations. (4) In between the large
616 collapses, microseismicity cluster are observed mostly at the southeast corner of the caldera.

617 **6 Conclusions**

618 Seismic and infrasound data reveal a complex deformation process at the Kīlauea summit during
619 the large seismic events, involving both inflation of the Halema'uma'u reservoir and a dominant
620 asymmetric slip along the northwest corner of the caldera. Near-field summit stations were
621 crucial to resolve the volumetric contribution in the early explosive events. Although the
622 inflation for the later collapses cannot be resolved, the fault geometry for the later collapses, i.e.,
623 slip along inward-dipping normal fault, were determined using two independent moment tensor
624 inversions. Infrasound data and particle motion analysis provide further constraints on source
625 migration pattern, source location and length of the lava lake conduit above the Halema'uma'u
626 reservoir. The asymmetric collapse at Kīlauea can explain other features including
627 microseismicity distribution and overestimation in geodetic modeling.

628 **Acknowledgments and Data**

629 We thank the editor and two anonymous reviewers for their constructive feedback on this
630 manuscript. We are deeply grateful for Luis Rivera for his insights and help on the teleseismic
631 moment tensor inversion, Greg Waite for providing the initial NPT infrasound data, and USGS –
632 Hawaiian Volcano Observatory for their dedication in maintaining the geophysical monitoring
633 network throughout the eruption. O.S. received funding from JSPS-KAKENHI (grant number:
634 JP20J01689). All seismic and infrasound data used in this study are available through the IRIS
635 webservices (<https://doi.org/10.7914/SN/HV>). The moment tensor catalogs are provided with
636 details in the Supporting Information.

637

638 **References**

- 639 Ágústsdóttir, T., Winder, T., Woods, J., White, R. S., Greenfield, T., & Brandsdóttir, B. (2019).
640 Intense Seismicity During the 2014–2015 Bárðarbunga-Holuhraun Rifting Event, Iceland,
641 Reveals the Nature of Dike-Induced Earthquakes and Caldera Collapse Mechanisms. *Journal*
642 *of Geophysical Research: Solid Earth*, 124(8), 8331–8357.
643 <https://doi.org/10.1029/2018JB016010>
- 644 [Alidibirov, M. A. \(1994\). A model for viscous magma fragmentation during volcanic blasts.](#)
645 [Bulletin of Volcanology, 56\(6\), 459-465.](#)
- 646 Alvizuri, C. R., Matoza, R. S., & Okubo, P. G. (2021). Earthquake collapse mechanisms and
647 periodic, migrating seismicity during the 2018 summit collapse at Kīlauea caldera. *Earth and*
648 *Planetary Science Letters*, 562, 116819.
- 649 Anderson, K. R., Poland, M. P., Johnson, J. H., & Miklius, A. (2015). Episodic Deflation-
650 Inflation Events at Kīlauea Volcano and Implications for the Shallow Magma System. In R.
651 Carey, V. Cayol, M. Poland, & D. Weis (Eds.), *Geophysical Monograph Series* (pp. 229–
652 250). John Wiley & Sons, Inc. <https://doi.org/10.1002/9781118872079.ch11>
- 653 Anderson, K. R., Johanson, I. A., Patrick, M. R., Gu, M., Segall, P., Poland, M. P., Montgomery-
654 Brown, E. K., & Miklius, A. (2019). Magma reservoir failure and the onset of caldera collapse

- 655 at Kīlauea Volcano in 2018. *Science*, 366(6470), eaaz1822.
 656 <https://doi.org/10.1126/science.aaz1822>
- 657 Averbuch, G., Assink, J. D., & Evers, L. G. (2020). Long-range atmospheric infrasound
 658 propagation from subsurface sources. *The Journal of the Acoustical Society of*
 659 *America*, 147(2), 1264-1274.
- 660 Baker, S., & Amelung, F. (2012). Top-down inflation and deflation at the summit of Kīlauea
 661 Volcano, Hawai‘i observed with InSAR. *Journal of Geophysical Research: Solid Earth*, 117,
 662 B12406. <https://doi.org/10.1029/2011JB009123>
- 663 Brissaud, Q., Martin, R., Garcia, R. F., & Komatitsch, D. (2017). Hybrid Galerkin numerical
 664 modelling of elastodynamics and compressible Navier–Stokes couplings: Applications to
 665 seismo-gravito acoustic waves. *Geophysical Journal International*, 210(2), 1047–1069.
 666 <https://doi.org/10.1093/gji/ggx185>
- 667 Butler, R. (2019). Composite Earthquake Source Mechanism for 2018 Mw 5.2–5.4 Swarm at
 668 Kīlauea Caldera: Antipodal Source Constraint. *Seismological Research Letters*.
 669 <https://doi.org/10.1785/0220180288>
- 670 Chapman, C. H., & Leaney, W. S. (2012). A new moment-tensor decomposition for seismic
 671 events in anisotropic media: Moment-tensor decomposition. *Geophysical Journal*
 672 *International*, 188(1), 343–370. <https://doi.org/10.1111/j.1365-246X.2011.05265.x>
- 673 Chouet, B. A., Dawson, P. B., James, M. R., & Lane, S. J. (2010). Seismic source mechanism of
 674 degassing bursts at Kīlauea Volcano, Hawaii: Results from waveform inversion in the 10–50 s
 675 band. *Journal of Geophysical Research*, 115(B9). <https://doi.org/10.1029/2009JB006661>
- 676 Contreras-Arratia, R., & Neuberg, J. W. (2020). Towards reconciling seismic and geodetic
 677 moment estimations: Case Bárðarbunga. *Journal of Volcanology and Geothermal*
 678 *Research*, 408, 107034.
- 679 Dawson, P. B., Benítez, M. C., Chouet, B. A., Wilson, D., & Okubo, P. G. (2010). Monitoring
 680 very-long-period seismicity at Kīlauea Volcano, Hawaii. *Geophysical Research Letters*,
 681 37(18). <https://doi.org/10.1029/2010GL044418>
- 682 [Dawson, P., & Chouet, B. \(2014\). Characterization of very-long-period seismicity accompanying](https://doi.org/10.1029/2014JB010441)
 683 [summit activity at Kīlauea Volcano, Hawai‘i: 2007–2013. *Journal of Volcanology and*](https://doi.org/10.1029/2014JB010441)
 684 [*Geothermal Research*, 278, 59-85.](https://doi.org/10.1029/2014JB010441)
- 685 Duputel, Z., & Rivera, L. (2019). The 2007 caldera collapse of Piton de la Fournaise volcano:
 686 Source process from very-long-period seismic signals. *Earth and Planetary Science Letters*,
 687 527, 115786. <https://doi.org/10.1016/j.epsl.2019.115786>
- 688 Fee, D., Garcés, M., Patrick, M., Chouet, B., Dawson, P., & Swanson, D. (2010). Infrasonic
 689 harmonic tremor and degassing bursts from Halema‘ūma‘u Crater, Kīlauea Volcano, Hawaii.
 690 *Journal of Geophysical Research*, 115(B11). <https://doi.org/10.1029/2010JB007642>
- 691 Fee, D., & Matoza, R. S. (2013). An overview of volcano infrasound: From hawaiian to plinian,
 692 local to global. *Journal of Volcanology and Geothermal Research*, 249, 123–139.
 693 <https://doi.org/10.1016/j.jvolgeores.2012.09.002>

- 694 [Flinders, A. F., Johanson, I. A., Dawson, P. B., Anderson, K. R., Haney, M. M., & Shiro, B. R.](#)
 695 [\(2020\). Very-Long-Period \(VLP\) Seismic Artifacts during the 2018 Caldera Collapse at](#)
 696 [Kīlauea, Hawai‘i. *Seismological Society of America*, 91\(6\), 3417-3432.](#)
- 697 Fontaine, F. R., Roullet, G., Hejrani, B., Michon, L., Ferrazzini, V., Barruol, G., Tkalčić, H.,
 698 Muro, A. D., Peltier, A., Reymond, D., Staudacher, T., & Massin, F. (2019). Very- and ultra-
 699 long-period seismic signals prior to and during caldera formation on La Réunion Island.
 700 *Scientific Reports*, 9(1), 1–15. <https://doi.org/10.1038/s41598-019-44439-1>
- 701 Fujiwara, Y., Yamasato, H., Shimbori, T., & Sakai, T. (2014). Characteristics of dilatational
 702 infrasonic pulses accompanying low-frequency earthquakes at Miyakejima Volcano, Japan.
 703 *Earth, Planets and Space*, 66(1), 1-12.
- 704 Fukao, Y., Sandanbata, O., Sugioka, H., Ito, A., Shiobara, H., Watada, S., & Satake, K. (2018).
 705 Mechanism of the 2015 volcanic tsunami earthquake near Torishima, Japan. *Science*
 706 *Advances*, 4(4), eaao0219. <https://doi.org/10.1126/sciadv.aao0219>
- 707 Gudmundsson, M. T., Jónsdóttir, K., Hooper, A., Holohan, E. P., Halldórsson, S. A., Ófeigsson,
 708 B. G., Cesca, S., Vogfjörð, K. S., Sigmundsson, F., Högnadóttir, T., Einarsson, P.,
 709 Sigmarsson, O., Jarosch, A. H., Jónasson, K., Magnússon, E., Hreinsdóttir, S., Bagnardi, M.,
 710 Parks, M. M., Hjörleifsdóttir, V., ... Aiuppa, A. (2016). Gradual caldera collapse at
 711 Bárðarbunga volcano, Iceland, regulated by lateral magma outflow. *Science*, 353(6296),
 712 aaf8988. <https://doi.org/10.1126/science.aaf8988>
- 713 Hejrani, B., & Tkalčić, H. (2020). Resolvability of the centroid-moment-tensors for shallow
 714 seismic sources and improvements from modelling high-frequency waveforms. *Journal of*
 715 *Geophysical Research: Solid Earth*, (February 2019), 1–13.
 716 <https://doi.org/10.1029/2020JB019643>
- 717 Holcomb, R. T. (1987). Eruptive history and long-term behavior of Kīlauea Volcano. *US Geol.*
 718 *Surv. Prof. Pap.*, 1350(1):261–350.
- 719 Johnson, J. B., & Lees, J. M. (2000). Plugs and chugs—seismic and acoustic observations of
 720 degassing explosions at Karymsky, Russia and Sangay, Ecuador. *Journal of Volcanology and*
 721 *Geothermal Research*, 101(1-2), 67-82.
- 722 Julian, B. R., Miller, A. D., & Foulger, G. R. (1998). Non-double-couple earthquakes 1. Theory.
 723 *Reviews of Geophysics*, 36(4), 525–549. <https://doi.org/10.1029/98RG00716>
- 724 Kanamori, H., & Anderson, D. L. (1975). Theoretical basis of some empirical relations in
 725 seismology. *Bulletin of the Seismological Society of America*, 65(5), 1073–1095.
- 726 Kanamori, H., & Brodsky, E. E. (2004). The physics of earthquakes. *Reports on Progress in*
 727 *Physics*, 67(8), 1429.
- 728 Kawakatsu, H. (1996). Observability of the isotropic component of a moment tensor.
 729 *Geophysical Journal International*, 126(2), 525–544. [https://doi.org/10.1111/j.1365-](https://doi.org/10.1111/j.1365-246X.1996.tb05308.x)
 730 [246X.1996.tb05308.x](https://doi.org/10.1111/j.1365-246X.1996.tb05308.x)
- 731 Kawakatsu, H., Kaneshima, S., Matsubayashi, H., Ohminato, T., Sudo, Y., Tsutsui, T., Uhira, K.,
 732 Yamasato, H., Ito, H., & Legrand, D. (2000). Aso94: Aso seismic observation with broadband
 733 instruments. *Journal of Volcanology and Geothermal Research*, 101(1–2), 129–154.
 734 [https://doi.org/10.1016/S0377-0273\(00\)00166-9](https://doi.org/10.1016/S0377-0273(00)00166-9)

- 735 Kobayashi, T., Ida, Y., & Ohminato, T. (2005). Small inflation sources producing seismic and
736 infrasonic pulses during the 2000 eruptions of Miyake-jima, Japan. *Earth and Planetary*
737 *Science Letters*, 240(2), 291–301. <https://doi.org/10.1016/j.epsl.2005.09.015>
- 738 Kumagai, H., & Chouet, B. A. (2000). Acoustic properties of a crack containing magmatic or
739 hydrothermal fluids. *Journal of Geophysical Research: Solid Earth*, 105(B11), 25493–25512.
- 740 Kumagai, H., Ohminato, T., Nakano, M., Ooi, M., Kubo, A., Inoue, H., & Oikawa, J. (2001).
741 Very-Long-Period Seismic Signals and Caldera Formation at Miyake Island, Japan. *Science*,
742 293(5530), 687–690. <https://doi.org/10.1126/science.1062136>
- 743 Liang, C., Crozier, J., Karlstrom, L., & Dunham, E. M. (2020). Magma Oscillations in a
744 Conduit-Reservoir System, Application to Very Long Period (VLP) Seismicity at Basaltic
745 Volcanoes: 2. Data Inversion and Interpretation at Kīlauea Volcano. *Journal of Geophysical*
746 *Research: Solid Earth*, 125(1), e2019JB017456. <https://doi.org/10.1029/2019JB017456>
- 747 Liang, C., & Dunham, E. M. (2020). Lava lake sloshing modes during the 2018 Kīlauea Volcano
748 eruption probe magma reservoir storativity. *Earth and Planetary Science Letters*, 535,
749 116110. <https://doi.org/10.1016/j.epsl.2020.116110>
- 750 Lin, G., Shearer, P. M., Matoza, R. S., Okubo, P. G., & Amelung, F. (2014). Three-dimensional
751 seismic velocity structure of Mauna Loa and Kilauea volcanoes in Hawaii from local seismic
752 tomography. *Journal of Geophysical Research: Solid Earth*, 119(5), 4377–4392.
753 <https://doi.org/10.1002/2013JB010820>
- 754 Lundgren, P. R., Bagnardi, M., & Dietterich, H. (2019). Topographic Changes During the 2018
755 Kīlauea Eruption from Single-pass Airborne InSAR. *Geophysical Research Letters*.
756 <https://doi.org/10.1029/2019GL083501>
- 757 Martire, L., Brissaud, Q., Lai, V. H., Garcia, R. F., Martin, R., Krishnamoorthy, S., et al. (2018).
758 Numerical simulation of the atmospheric signature of artificial and natural seismic events.
759 *Geophysical Research Letters*, 45, 12,085–12,093. <https://doi.org/10.1029/2018GL080485>
- 760 Morrissey, M. M., & Chouet, B. A. (2001). Trends in long-period seismicity related to magmatic
761 fluid compositions. *Journal of volcanology and geothermal research*, 108(1-4), 265–281.
- 762 Neal, C. A., Brantley, S. R., Antolik, L., Babb, J. L., Burgess, M., Calles, K., Cappos, M.,
763 Chang, J. C., Conway, S., Desmither, L., Dotray, P., Elias, T., Fukunaga, P., Fuke, S.,
764 Johanson, I. A., Kamibayashi, K., Kauahikaua, J., Lee, R. L., Pekalib, S., ... Damby, D.
765 (2019). The 2018 rift eruption and summit collapse of Kīlauea Volcano. *Science*, 363(6425),
766 367–374. <https://doi.org/10.1126/science.aav7046>
- 767 Orr, T. R., Thelen, W. A., Patrick, M. R., Swanson, D. A., & Wilson, D. C. (2013). Explosive
768 eruptions triggered by rockfalls at Kīlauea volcano, Hawai‘i. *Geology*, 41(2), 207–210.
769 <https://doi.org/10.1130/G33564.1>
- 770 Patrick, M. R., Harris, A. J. L., Ripepe, M., Dehn, J., Rothery, D. A., & Calvari, S. (2007).
771 Strombolian explosive styles and source conditions: Insights from thermal (FLIR) video.
772 *Bulletin of Volcanology*, 69(7), 769–784. <https://doi.org/10.1007/s00445-006-0107-0>
- 773 Patrick, M. R., Anderson, K. R., Poland, M. P., Orr, T. R., & Swanson, D. A. (2015). Lava lake
774 level as a gauge of magma reservoir pressure and eruptive hazard. *Geology*, 43(9), 831–834.
775 <https://doi.org/10.1130/G36896.1>

- 776 Patrick, M. R., Dietterich, H. R., Lyons, J. J., Diefenbach, A. K., Parcheta, C., Anderson, K. R.,
 777 Namiki, A., Sumita, I., Shiro, B., & Kauahikaua, J. P. (2019). Cyclic lava effusion during the
 778 2018 eruption of Kīlauea Volcano. *Science*, 366(6470).
 779 <https://doi.org/10.1126/science.aay9070>
- 780 Poland, M. P., Miklius, A., & Montgomery-Brown, E. K. (2014). Magma supply, storage, and
 781 transport at shield-stage Hawaiian volcanoes. In *Magma supply, storage, and transport at*
 782 *shield-stage Hawaiian volcanoes* (USGS Numbered Series No. 1801–5; Professional Paper,
 783 Vols. 1801–5, p. 56). U.S. Geological Survey. <https://doi.org/10.3133/pp18015>
- 784 Sandanbata, O., Kanamori, H., Rivera, L., Zhan, Z., Watada, S., & Satake, K. (2021). Moment
 785 Tensors of Ring-Faulting at Active Volcanoes: Insights into Vertical-CLVD Earthquakes at
 786 the Sierra Negra Caldera, Galápagos Islands. *Journal of Geophysical Research: Solid Earth*,
 787 e2021JB021693.
- 788 Segall, P., Anderson, K. R., Johanson, I., & Miklius, A. (2019). Mechanics of Inflationary
 789 Deformation During Caldera Collapse: Evidence From the 2018 Kīlauea Eruption.
 790 *Geophysical Research Letters*, 46(21), 11782–11789. <https://doi.org/10.1029/2019GL084689>
- 791 Segall, P., Anderson, K. R., Pulvirenti, F., Wang, T., & Johanson, I. (2020). Caldera Collapse
 792 Geometry Revealed by Near-Field GPS Displacements at Kīlauea Volcano in 2018.
 793 *Geophysical Research Letters*, 47(15), e2020GL088867.
 794 <https://doi.org/10.1029/2020GL088867>
- 795 Shelly, D. R., & Thelen, W. A. (2019). Anatomy of a Caldera Collapse: Kīlauea 2018 Summit
 796 Seismicity Sequence in High Resolution. *Geophysical Research Letters*, 46(24), 14395–
 797 14403. <https://doi.org/10.1029/2019GL085636>
- 798 [Spieler, O., Kennedy, B., Kueppers, U., Dingwell, D. B., Scheu, B., & Taddeucci, J. \(2004\). The](#)
 799 [fragmentation threshold of pyroclastic rocks. *Earth and Planetary Science Letters*, 226\(1-2\),](#)
 800 [139-148.](#)
- 801 Taddeucci, J., Scarlato, P., Capponi, A., Bello, E. D., Cimorelli, C., Palladino, D. M., &
 802 Kueppers, U. (2012). High-speed imaging of Strombolian explosions: The ejection velocity of
 803 pyroclasts. *Geophysical Research Letters*, 39(2). <https://doi.org/10.1029/2011GL050404>
- 804 Tepp, G., Hotovec-Ellis, A., Shiro, B., Johanson, I., Thelen, W., & Haney, M. M. (2020).
 805 Seismic and geodetic progression of the 2018 summit caldera collapse of Kīlauea volcano.
 806 *Earth and Planetary Science Letters*, 540, 116250. <https://doi.org/10.1016/j.epsl.2020.116250>
- 807 [USGS Hawaiian Volcano Observatory \(HVO\). \(1956\). Hawaiian Volcano Observatory Network.](#)
 808 [International Federation of Digital Seismograph Networks. *https://doi.org/10.7914/SN/HV*](#)
- 809 Wielandt, E., & Forbriger, T. (1999). Near-field seismic displacement and tilt associated with the
 810 explosive activity of Stromboli. *Annals of Geophysics*, 42(3).
- 811 Zhao, L.-S., & Helmberger, D. V. (1994). Source estimation from broadband regional
 812 seismograms. *Bulletin of the Seismological Society of America*, 84(1), 91–104.
- 813 Zhu, L., & Ben-Zion, Y. (2013). Parametrization of general seismic potency and moment tensors
 814 for source inversion of seismic waveform data. *Geophysical Journal International*, 194(2),
 815 839–843. <https://doi.org/10.1093/gji/ggt137>

816 Zhu, L., & Helmberger, D. V. (1996). Advancement in source estimation techniques using
817 broadband regional seismograms. *Bulletin of the Seismological Society of America*, 86(5),
818 1634–1641.

819 Zhu, L., & Rivera, L. A. (2002). A note on the dynamic and static displacements from a point
820 source in multilayered media: A note on the dynamic and static displacements from a point
821 source. *Geophysical Journal International*, 148(3), 619–627. [https://doi.org/10.1046/j.1365-
822 246X.2002.01610.x](https://doi.org/10.1046/j.1365-246X.2002.01610.x)

823
824

825

826 **References for supporting information**

827 Duputel, Z., Rivera, L., Kanamori, H., & Hayes, G. (2012). W phase source inversion for
828 moderate to large earthquakes (1990–2010). *Geophysical Journal International*, 189(2),
829 1125–1147. <https://doi.org/10.1111/j.1365-246X.2012.05419.x>

830 Hayes, G. P., Rivera, L., & Kanamori, H. (2009). Source Inversion of the W-Phase: Real-time
831 Implementation and Extension to Low Magnitudes. *Seismological Research Letters*, 80(5),
832 817–822. <https://doi.org/10.1785/gssrl.80.5.817>

833 Kanamori, H., & Rivera, L. (2008). Source inversion of W phase: Speeding up seismic tsunami
834 warning. *Geophysical Journal International*, 175(1), 222–238. [https://doi.org/10.1111/j.1365-
835 246X.2008.03887.x](https://doi.org/10.1111/j.1365-246X.2008.03887.x)

836 Sandanbata, O., Kanamori, H., Rivera, L., Zhan, Z., Watada, S., & Satake, K. (2021). Moment
837 tensors of ring-faulting at active volcanoes: Insights into vertical-CLVD earthquakes at the
838 Sierra Negra caldera, Galapagos Islands. *Earth and Space Science Open Archive; Earth and
839 Space Science Open Archive*. <https://doi.org/10.1002/essoar.10505947.1>

**Inflation and Asymmetric Collapse at Kilauea Summit
during the 2018 Eruption from Seismic and Infrasound Analyses**

Voon Hui Lai^{1,2}, Zhongwen Zhan¹,
Quentin Brissaud^{1,3}, Osamu Sandanbata⁴ and Meghan S. Miller²

¹Seismological Laboratory, California Institute of Technology, USA.

²Research School of Earth Sciences, The Australian National University, Australia

³Norwegian Seismic Array (NORSAR), Norway.

⁴National Research Institute for Earth Science and Disaster Resilience, Japan.

Corresponding author: Voon Hui Lai (voonhui.lai@anu.edu.au)

Contents of this file

Text S1
Text S2
Figures S1 to S18

Additional Supporting Information

Captions for Datasets S1 to S2

Introduction

Supporting information contains the description of moment tensor decomposition for very long period teleseismic inversion (Text S1), the procedure for the teleseismic inversion (Text S2), supplementary figures referenced in the main text (Figures S1 to S16), and captions for the two moment tensor catalogs produced using the local and global data (Dataset S1 and S2).

Text S1. Moment tensor decomposition for very long period teleseismic inversion

In Section 5.2 of Main Text, we decompose moment tensors into three components, vertical-CLVD (vCLVD), vertical dip-slip (DS), and vertical strike-slip (SS) components, following Sandanbata et al. (2021). First, we define three moment scales corresponding to isotropic (*ISO*), vertical-CLVD (vCLVD), and difference (*D*) components with the three diagonal elements (M_{rr} , $M_{\theta\theta}$, and $M_{\phi\phi}$):

$$M_{vCLVD} = \frac{1}{3}(2M_{rr} - M_{\theta\theta} - M_{\phi\phi}), \quad (1)$$

and

$$M_D = \frac{1}{2}(M_{\theta\theta} - M_{\phi\phi}). \quad (2)$$

Note that ring-faulting has no isotropic component is contained ($M_{ISO} = M_{rr} + M_{\theta\theta} + M_{\phi\phi} = 0$). Using the two moment scales (M_{vCLVD} and M_D) and the non-diagonal elements ($M_{r\theta}$, $M_{r\phi}$, and $M_{\theta\phi}$), the moment tensor is decomposed into three components, vCLVD, SS, and DS, respectively, in the following form:

$$\mathbf{M} = \mathbf{M}_{vCLVD} + \mathbf{M}_{SS} + \mathbf{M}_{DS}, \quad (3)$$

where

$$\mathbf{M}_{vCLVD} = M_{vCLVD} \begin{bmatrix} -1 & & \\ 0 & 0.5 & \\ 0 & 0 & 0.5 \end{bmatrix}, \quad (4)$$

$$\mathbf{M}_{SS} = \mathbf{M}_D + \mathbf{M}_{\theta\phi} = M_D \begin{bmatrix} 0 & & \\ 0 & 1 & \\ 0 & 0 & -1 \end{bmatrix} + M_{\theta\phi} \begin{bmatrix} 0 & & \\ 0 & 0 & \\ 0 & 1 & 0 \end{bmatrix}, \quad (5)$$

and

$$\mathbf{M}_{DS} = \mathbf{M}_{r\theta} + \mathbf{M}_{r\phi} = M_{r\theta} \begin{bmatrix} 0 & & \\ 1 & 0 & \\ 0 & 0 & 0 \end{bmatrix} + M_{r\phi} \begin{bmatrix} 0 & & \\ 0 & 0 & \\ 1 & 0 & 0 \end{bmatrix}. \quad (6)$$

The sign of M_{vCLVD} in Equation (3) depends on the type of vertical-CLVD component: $M_{vCLVD} > 0$ for vertical-T CLVD, and $M_{vCLVD} < 0$ for vertical-P CLVD. Then the moment

scales of the SS and DS components are defined by $M_{SS} = \sqrt{M_D^2 + M_{\theta\phi}^2}$, and $M_{DS} =$

$\sqrt{M_{r\theta}^2 + M_{r\phi}^2}$, respectively.

Using the two components that are resolvable from very long-period seismic waves at far field, i.e., \mathbf{M}_{vCLVD} and \mathbf{M}_{SS} , the resolvable moment tensor is defined as

$$\mathbf{M}_{RES} = \mathbf{M}_{vCLVD} + \mathbf{M}_{SS}. \quad (7)$$

Using the moment scales of the two resolvable components, the CLVD ratio (k_{CLVD}) is defined as

$$k_{CLVD} = \frac{|M_{vCLVD}|}{|M_{vCLVD}| + M_{SS}} \times 100 [\%], \quad (8)$$

which is a function of the arc angle of the ring fault (Fig. S11c). The P-axis axis of \mathbf{M}_{SS} can be used as a proxy of the orientation of the fault plane measured at the midpoint of the curved fault (Figure S11d).

Text S2. Procedure for very long period teleseismic inversion

In Section 5.2 of Main Text, to estimate source parameters of the ring fault, we performed the moment tensor inversion for the 50 collapse events using very long period teleseismic waveforms with the zero-trace constraint ($M_{ISO} = M_{rr} + M_{\theta\theta} + M_{\phi\phi} = 0$). We use the W-phase code for the inversion process, including the filtering, data screening and computation of the Green's functions (Kanamori and Rivera, 2008; Hayes et al., 2009; Duputel et al., 2012). The Green's functions are normal modes generated from 1D PREM model, with waveforms filtered between 0.005 and 0.01 Hz. The centroid location is simply assumed at the caldera center at 0.5 km depth below the solid surface, as a case study demonstrated that these resolvable components are well-constrained even with uncertainty in centroid location and depth (Sandarbata et al., 2021). We used the vertical component of broad-band seismic records at stations ranging from 15° to 90° in epicentral distance. Using \mathbf{M}_{RES} extracted from the obtained moment tensor, we determined k_{CLVD} and the P-axis direction of \mathbf{M}_{SS} (Figures S13, and red dots in Figure S14). To consider the bias in the estimation of \mathbf{M}_{RES} caused by a positive isotropic source close to the ring fault, we additionally conducted the inversion with the constraint of $M_{ISO} = 4.23 \times 10^{16}$ Nm. We found that the positive isotropic source only reduced our estimate of k_{CLVD} (black dots Figure S14).

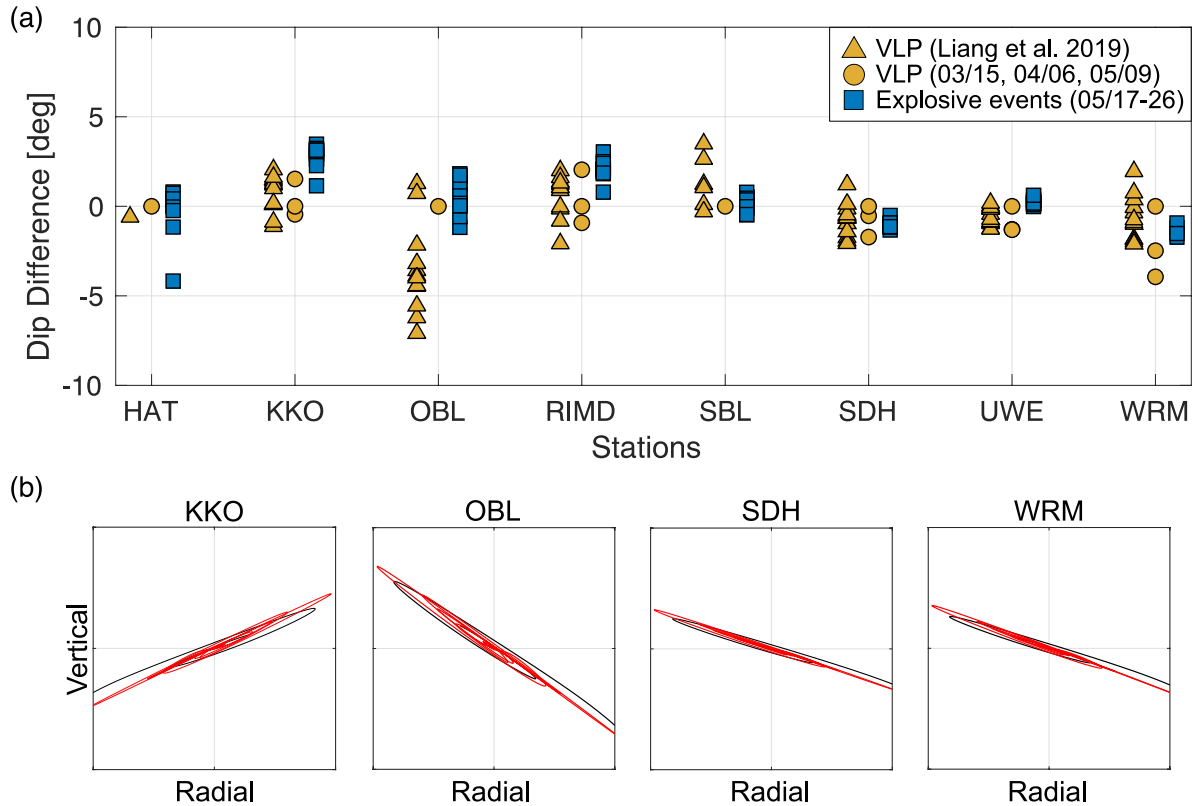


Figure S1:

(a) Graph shows the difference in measured dip of the reference Very Long Period (VLP) event on 05/09 to other VLP events prior to 05/17 (i.e., 03/15, 04/06 and events studied by Liang et al. (2019) between 05/03 and 05/07) and the explosive seismic events (05/17 to 05/26). Dip is measured from the radial and vertical particle motions filtered at 0.02 – 0.05 Hz. The radial component is obtained by rotating the horizontal particle motions according to the observed azimuths in Figure 2. The difference in dip among events is small, indicating a great overlapping of particle motion and that the seismic source for the events is at similar depth. Station OBL shows the greatest variation due to close proximity to the source and steep topography. (b) Plots show the comparison of particle motions from the reference VLP event (black) to explosive event 2 (05/17b; red) at station KKO, OBL, SDH, and WRM.

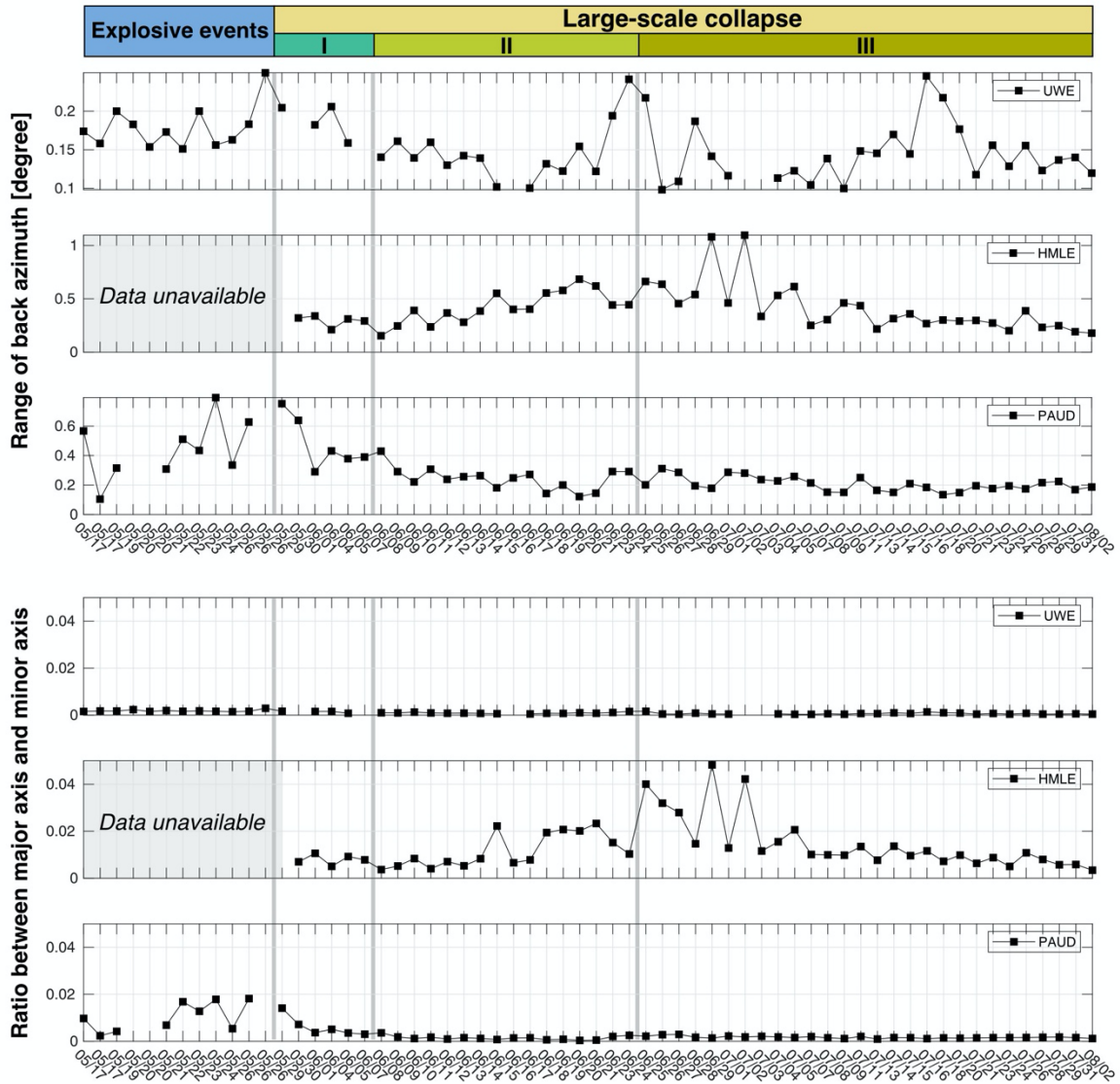
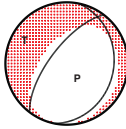


Figure S2:

Top graph shows the range of back azimuths measured using bootstrapping method for each station. Overall, the particle motions have a small range (generally less than 0.5 degree). Bottom graph shows the ratio between the major axis and minor axis of the ellipsoidal particle motion. Small ratio indicates high rectilinearity. Measurements with larger than average ratio also have a large range in the back azimuths measurement.



Ev#2 • UTC 2018/05/17 14:04 • Depth 0.9 km • Surface Wave Displacement (0.03–0.08 Hz)
 Strike 48 Dip 42 Rake -89 • Mw 4.61 • Source Duration 15 sec (triangle)
 Global CMT solution

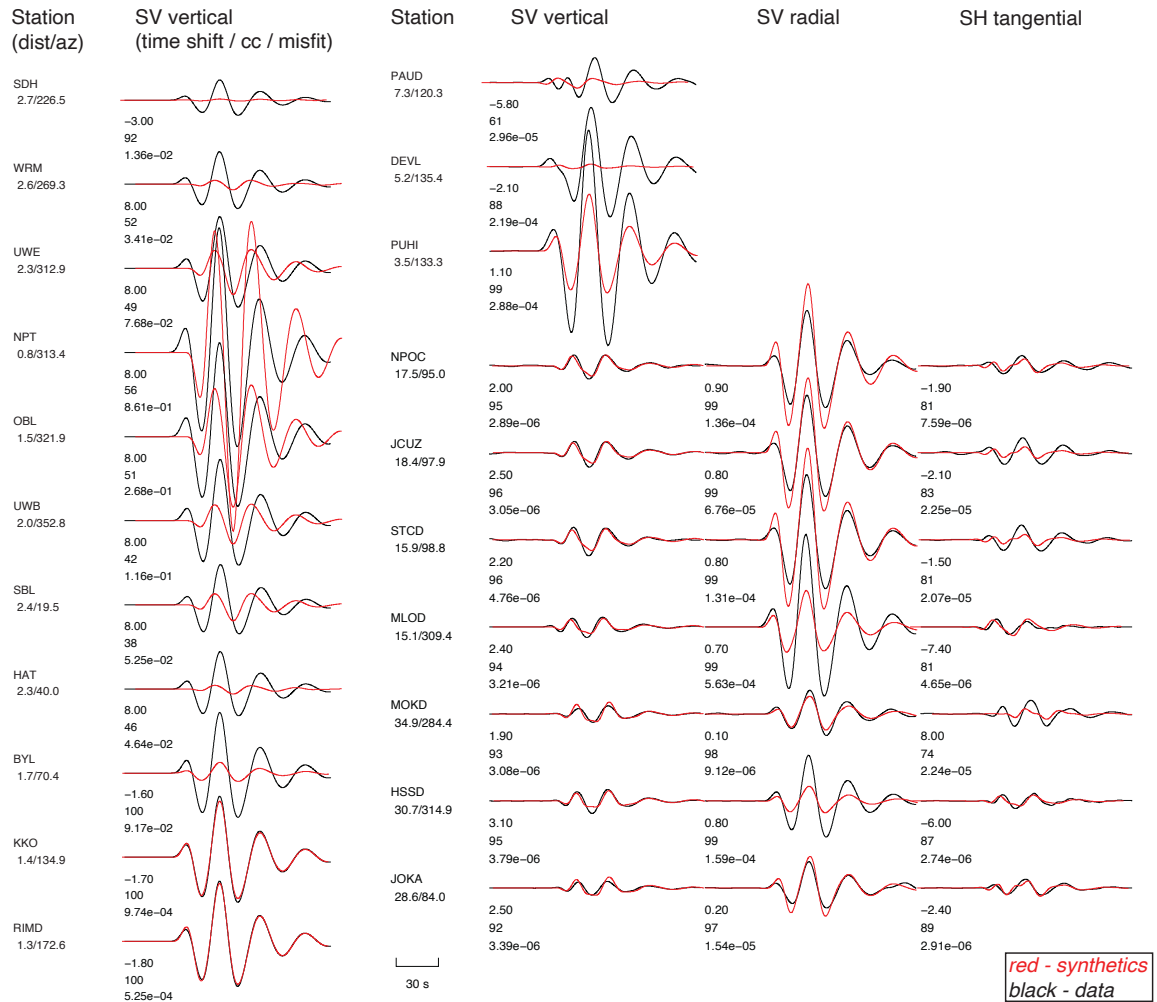
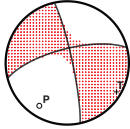


Figure S3:

Figure shows the waveform fitting of synthetics (red) from the global Centroid Moment Tensor (GCMT) solution to the observed data (black) for explosive event 2 (2018/05/17b). The waveforms are surface wave displacement filtered at 0.03 – 0.08 Hz. The waveforms are allowed to shift in time to maximize the correlation coefficient value. The GCMT solution fits the regional waveforms but does not fit the vertical components from stations less than 10 km away from the summit.



Ev#2 • UTC 2018/05/17 14:04 • Depth 0.9 km • Surface Wave Displacement (0.03–0.08 Hz)
 Strike 256 Dip 71 Rake -7 • Mw 4.83 • Source Duration 15 sec (triangle)
 DC 73% • CLVD 27% (Deviatoric solution)

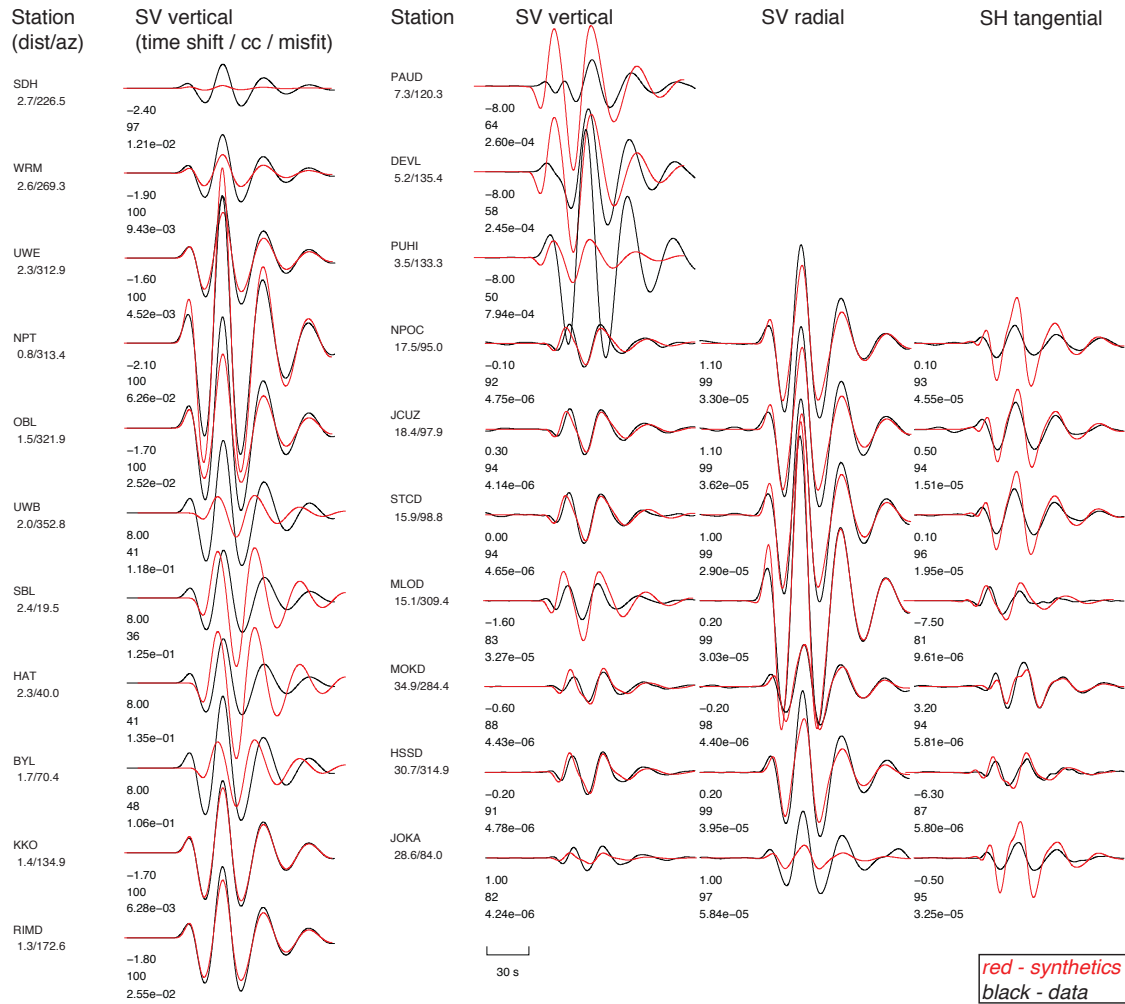
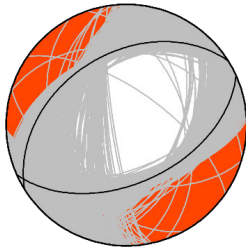


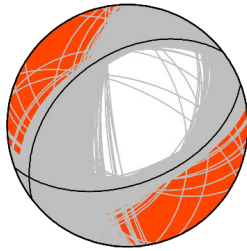
Figure S4:

Figure shows the waveform fitting of synthetics (red) from the best-fitting deviatoric solution inverted using gCAP to the observed data (black) for explosive event 2 (2018/05/17b). The waveforms are surface wave displacement filtered at 0.03 – 0.08 Hz. The deviatoric solution fits the regional waveforms but does not fit all the vertical components from stations less than 10 km away from the summit.

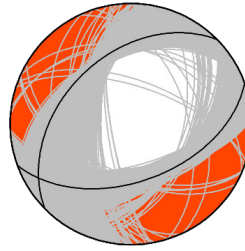
Event 1: 05/17a
Strike: 66
Rake: -85
Dip: 50



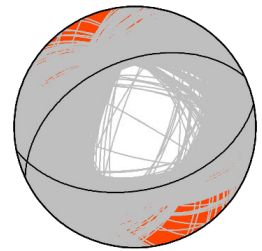
Event 2: 05/17b
Strike: 70
Rake: -79
Dip: 50



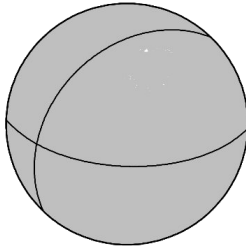
Event 3: 05/19
Strike: 70
Rake: -71
Dip: 51



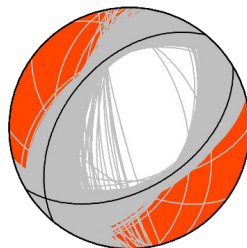
Event 4: 05/20a
Strike: 79
Rake: -80
Dip: 46



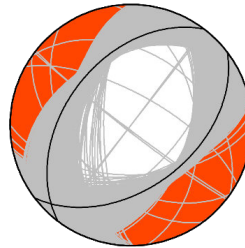
Event 5: 05/20b
Strike: 92
Rake: -62
Dip: 61



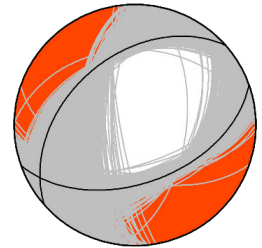
Event 6: 05/21
Strike: 59
Rake: -76
Dip: 47



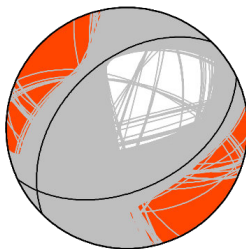
Event 7: 05/22
Strike: 52
Rake: -79
Dip: 47



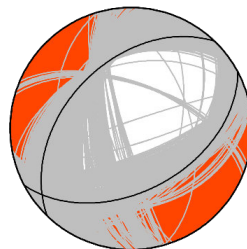
Event 8: 05/23
Strike: 70
Rake: -76
Dip: 50



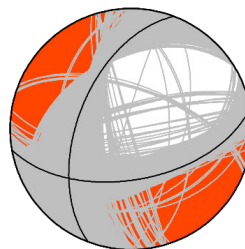
Event 9: 05/24
Strike: 65
Rake: -76
Dip: 47



Event 10: 05/26a
Strike: 62
Rake: -77
Dip: 47



Event 11: 05/26b
Strike: 80
Rake: -46
Dip: 55



Event 12: 05/26c
Strike: 70
Rake: -63
Dip: 50

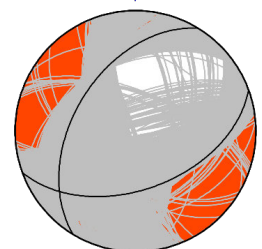


Figure S5:

Figure shows the bootstrapping results of the strike, rake, and dip for explosive events between 05/17 and 05/26. The focal mechanism shows the double-couple contribution, the nodal planes from the bootstrapping (grey), and the preferred nodal planes (black) from the best-fitting full moment tensor solution. All events, except for Event 4 and 5, show consistent strike, rake, and dip.

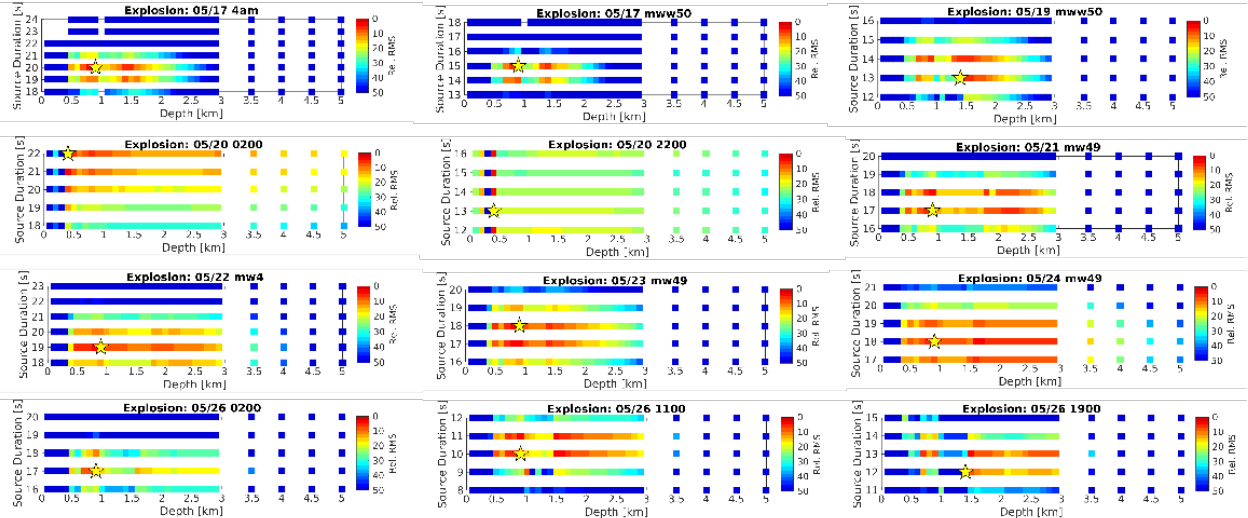


Figure S6:

Figure shows the misfits of the gCAP full moment tensor solutions for a range of source duration and depth for the explosive events between 05/17 and 05/26. The root mean square (RMS) misfit is scaled to the best-fit solution for each event, which is marked by the yellow star. Most events prefer depths between 0.7 and 2.0 km, with the best solution 900 m from the surface. The preferred source duration is independent for each event. Event 4 and 5 (05/20) have complicated waveforms hence resulting in poor grid search results.

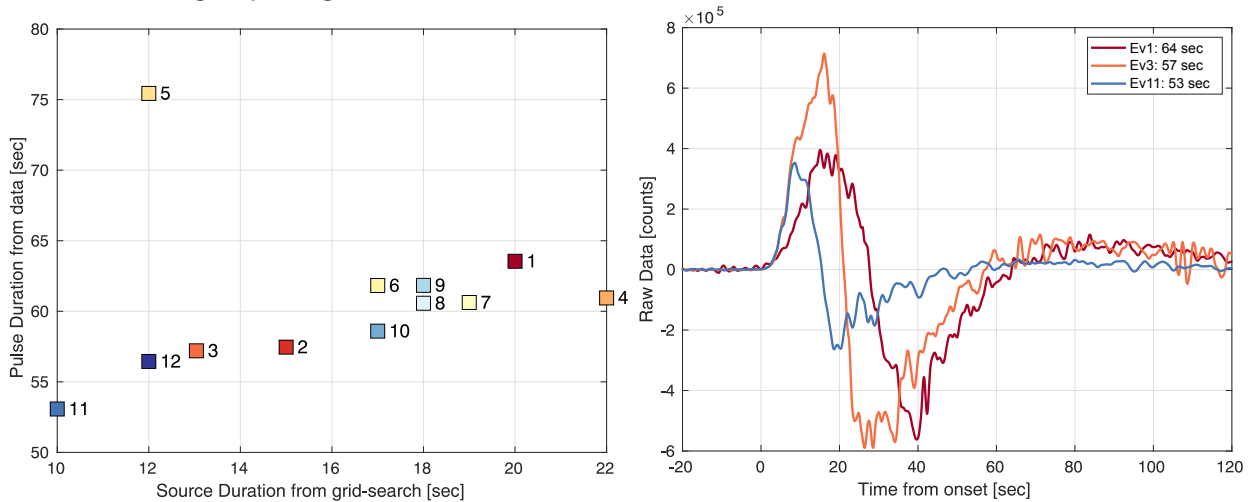


Figure S7:

Left graph shows a strong correlation between the measured pulse duration from raw data to the preferred source duration from grid-search for each explosive events. Event 4 and 5 do not fit the trend as their moment tensor solutions are poorly constrained. Right plot shows the raw waveform for event 1, 3 and 11. The pulse duration is measured from the first zero crossing before onset to the third zero crossing at the end of the signal.

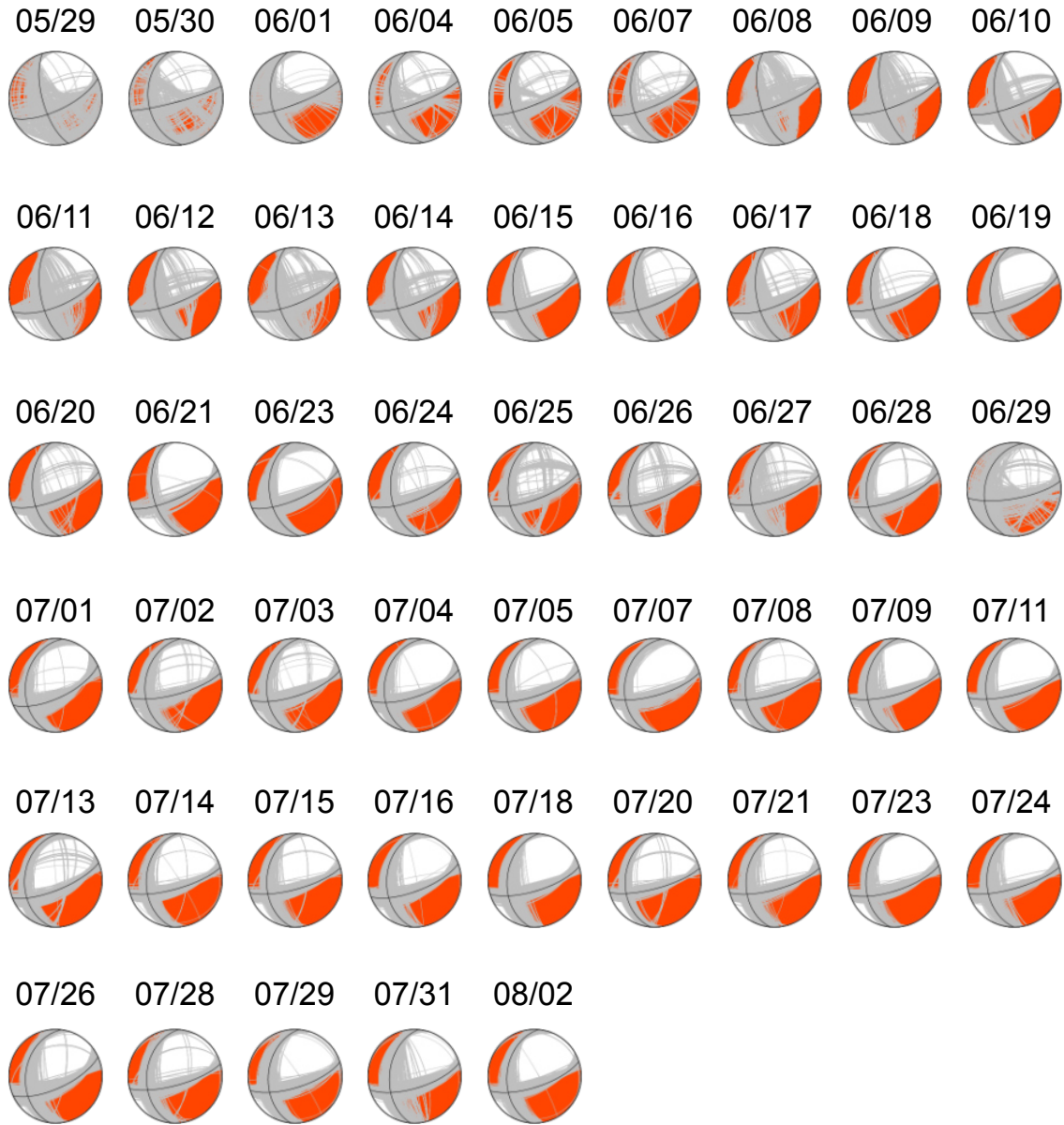


Figure S8:

Figure shows the bootstrapping results of the strike, rake, and dip for large collapse events between 05/29 and 08/02. The focal mechanism shows the double-couple contribution, the nodal planes from the bootstrapping (grey), and the preferred nodal planes (black) from the best-fitting full moment tensor solution. Despite the small number of stations, the bootstrapping results show consistent strike, rake, and dip for most events, indicating good constraint on the focal mechanism.

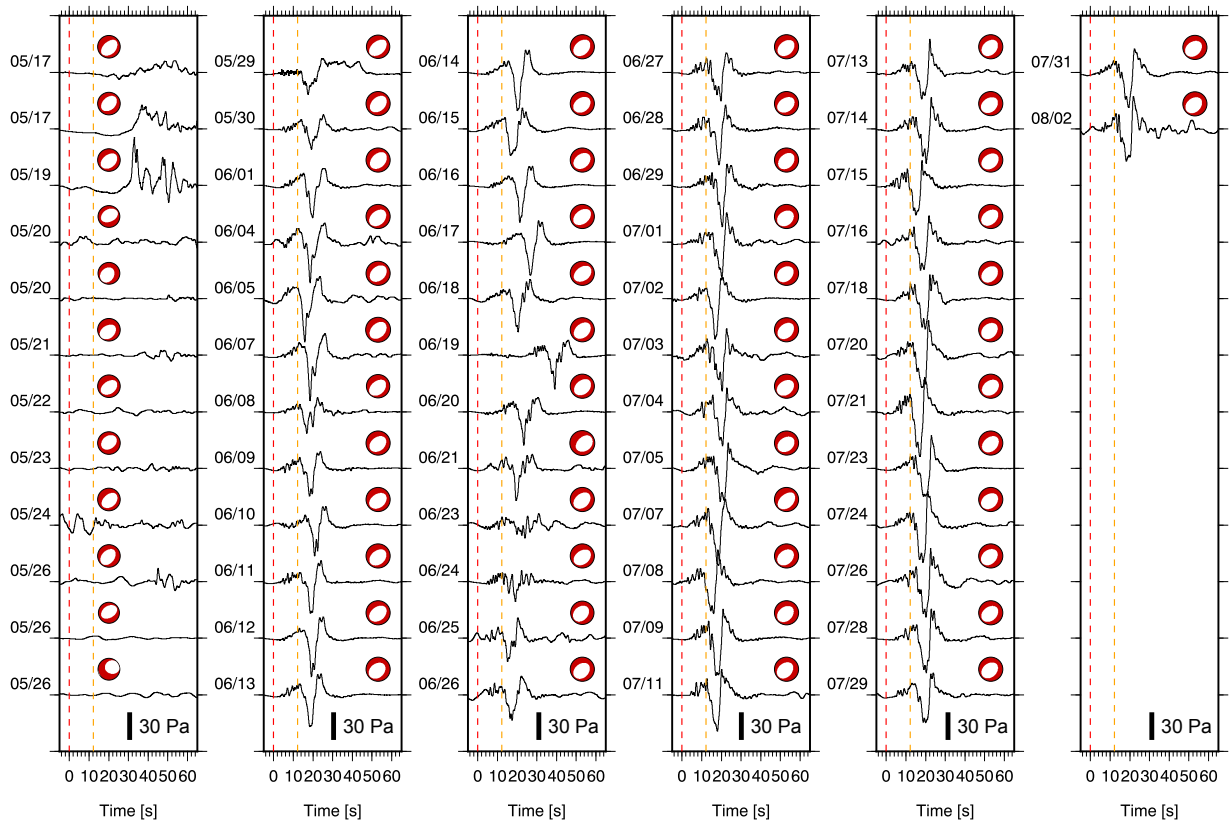


Figure S9:

Figure shows infrasound data recorded at AHUD and the Global Centroid Moment Tensor (GCMT) solutions for the 62 summit events. The infrasound data is deconvolved with the instrument response (last accessed July 2021) and filtered at 0.04 to 1 Hz. The data are plotted on the same amplitude scale. The red dashed line is a marker for origin time from catalog and the orange dashed line marks the expected arrival time of the infrasonic pulse traveling at acoustic speed (~ 340 m/s) from source to sensor. The GCMT solutions are similar for all events. The infrasound data, on the other hand, have two distinct patterns. Data from 05/17 to 05/26 vary greatly between each event and have no clear arrival at the expected time. Data from 05/29 onwards have a distinct high frequency signal followed by a strong downward pulse which travels at acoustic speed. Events 06/17 and 06/19 have complicated subevents and the catalog origin time is assigned to the first subevent. The delayed arrivals in comparison to other events, suggest the later subevent is responsible for the infrasound signal.

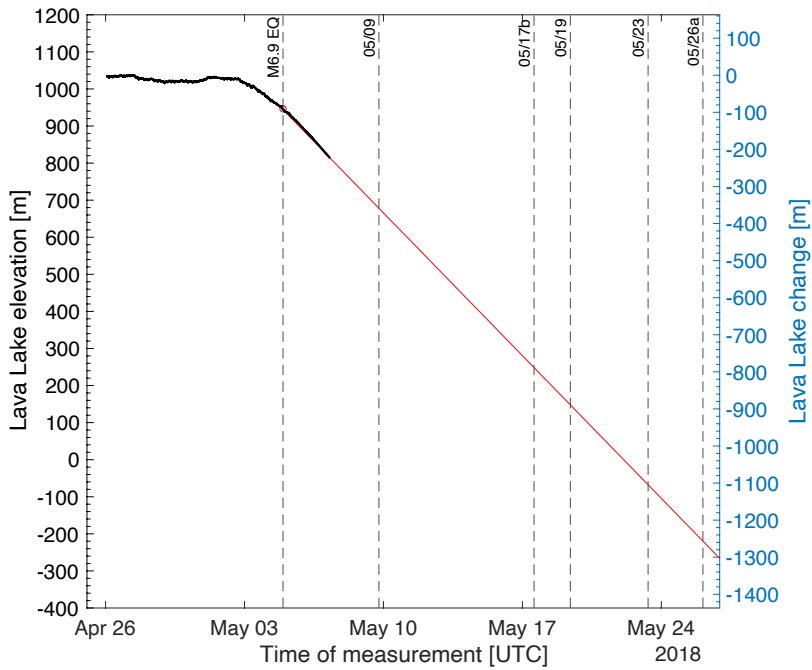
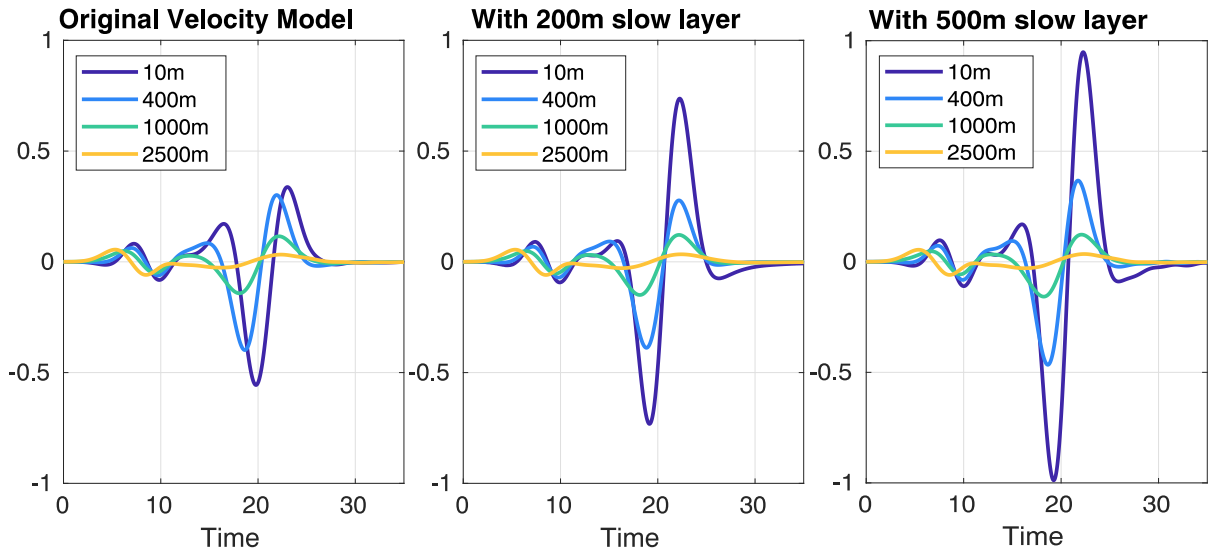


Figure S10:

Plot shows the lava lake elevation data measured from continuous laser rangefinder collected by USGS-HVO (black) and the estimated lava lake elevation change based on a constant draining rate of 2.2 meter per hour since the large M6.9 earthquake. By the end of the explosive events, the lava lake has dropped to a depth of ~1260 m. The data from the laser rangefinder can be obtained here: [doi:10.5066/P9MJY24N](https://doi.org/10.5066/P9MJY24N)

(a) Comparison of Sources at different depths for three velocity models



(b) Comparison of Sources at same depths for three velocity models

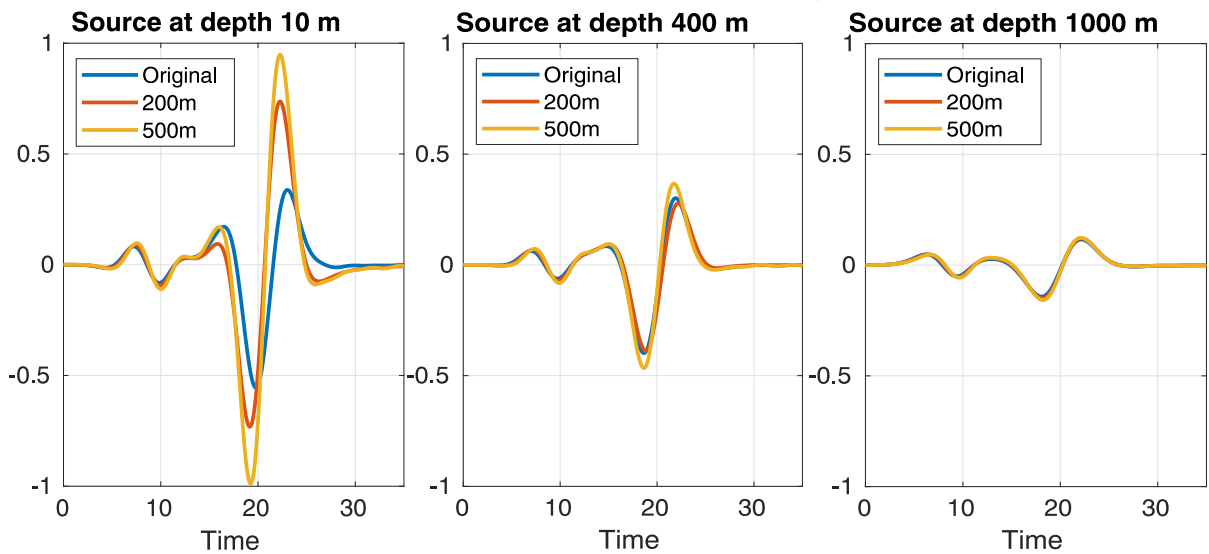


Figure S11:

(a) Plot shows the comparison of synthetics generated using the collapse solution (normal-faulting) at various depths with the 1-D velocity model used in the seismic inversions, and two modified velocity models in which the top 200 and 500 m are replaced with a slow layer. (b) Plot shows similar comparison but for synthetics at fixed source depth for the three velocity models. The synthetics show that the amplitude ratio between the acoustic and Rayleigh pulse is stronger for source at shallower depth. The amplitude ratio increases as well when there is a slow surface layer, particularly for sources at shallower depth. We can exclude sources at depth greater than 1 km, as the amplitude ratio is close to 1, which is not observed in data, and the ratio does not change greatly with velocity models.

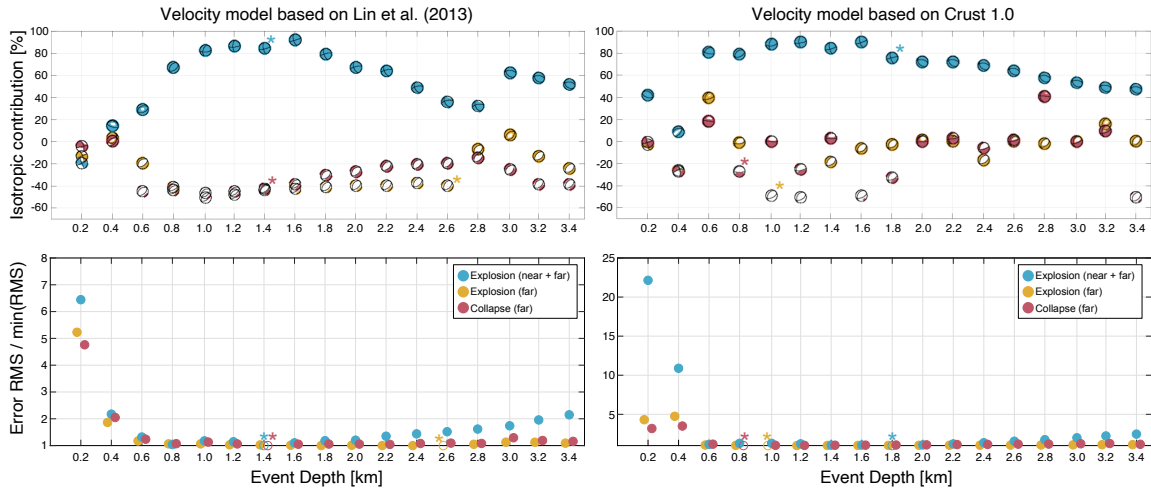


Figure S12:

Figure shows the effect of depth and availability of near field stations on the recovered full moment tensor solutions. We solve for the full moment tensor solutions using gCAP for three types of events: (blue) explosive event on May 17 (event 1) using all near field and regional stations; (yellow) same explosive event with regional stations only; and (pink) collapse event on July 20 with regional stations. Top row shows the isotropic contribution of the recovered moment tensors for event depths between 0.2 and 3.4 km for the two velocity models derived from Lin et al. (2013; this study) and Crust 1.0. Bottom row shows the distribution of error RMS with depth. The error RMS is normalized with the minimum RMS within each event category. The points have a slight offset for visual clarity. The best solutions have a normalized error RMS of 1 and are marked with color-coded asterisks. We found that the best moment tensor solutions without near-field stations consistently prefer deeper depths and have a negative isotropic contribution. Full moment tensor solutions for shallow depths are unstable due to the weak excitation of isotropic and dip-slip components.

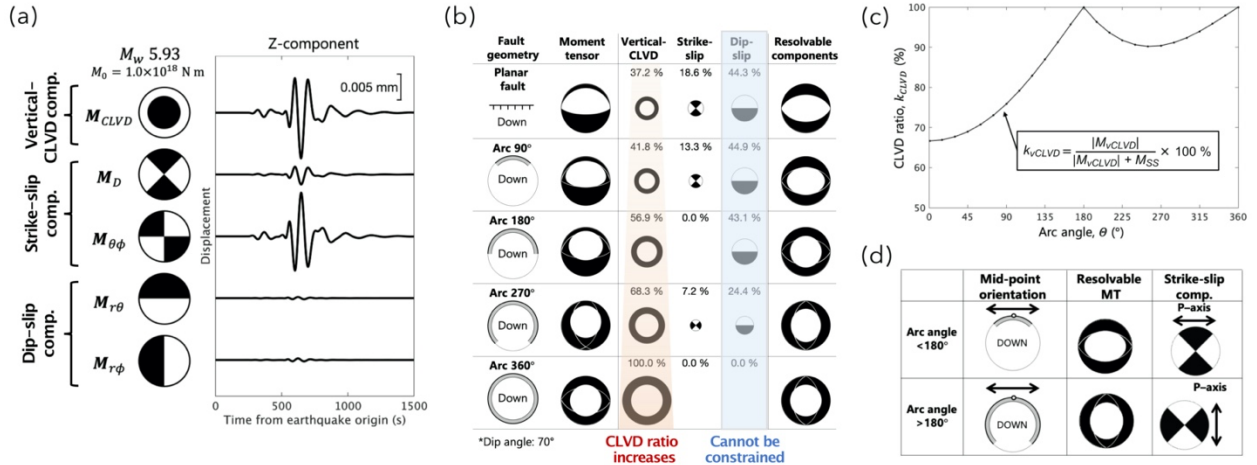


Figure S13:

(a) Figure illustrates that for a shallow earthquake, the vertical-CLVD and strike-slip components excite long period surface waves observable at teleseismic distances but not the dip-slip components ($M_{r\theta}$ and $M_{r\phi}$).

(b) Figure shows the theoretical moment tensor solution, their respective vertical-CLVD, strike-slip and dip-slip contributions, and resolvable moment tensor from teleseismic surface waves for planar fault slip, partial ring-fault slips and complete ring-fault slip. The CLVD ratio k_{CLVD} is sensitive to the arc angle of the ring fault that has slipped. k_{CLVD} is minimum (66.7%) for a linear fault. As the arc angle increases, M_{vCLVD} increases while M_{SS} decreases, resulting in an increase in k_{CLVD} . k_{CLVD} is maximum (100%) when the arc angle is 180° or 360° because M_{SS} is zero. The dip-slip components are not resolved by teleseismic surface waves.

(c) Graph shows the relationship between k_{CLVD} and the arc angle of the ring-fault slip, estimated from synthetic test. $k_{CLVD} < \sim 80\%$ corresponds to small arc angle ($< 180^\circ$).

(d) Figure shows two examples of caldera block dropping inward with partial ring-fault slip where the arc angles are $< 180^\circ$ and $> 180^\circ$. The resolvable moment tensors look similar but their respective strike-slip component shows different orientation for the P-axis. For arc angle less than 180°, the P-axis is parallel to the tangent at the mid-point of the fault; for arc angle more than 180°, the P-axis is perpendicular to the tangent at the mid-point.

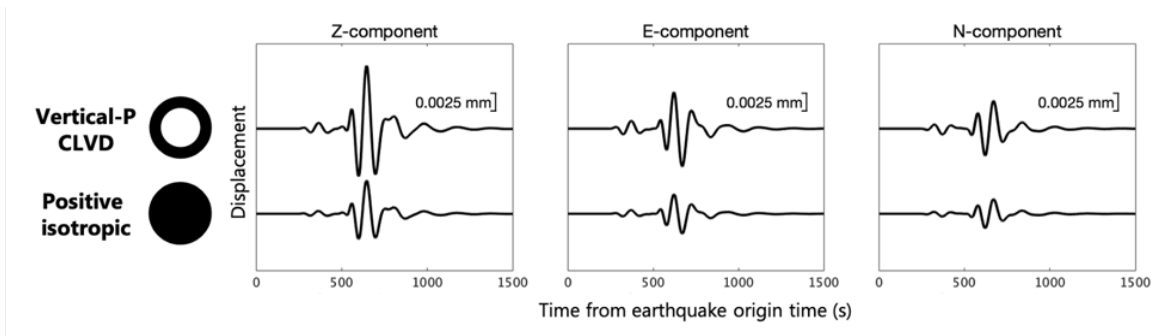


Figure S14:

Figure shows the similarity of teleseismic surface wave displacements for all three components produced by vertical-P CLVD and positive isotropic mechanisms, indicating a strong trade-off in resolving the vertical-P CLVD and isotropic contributions.

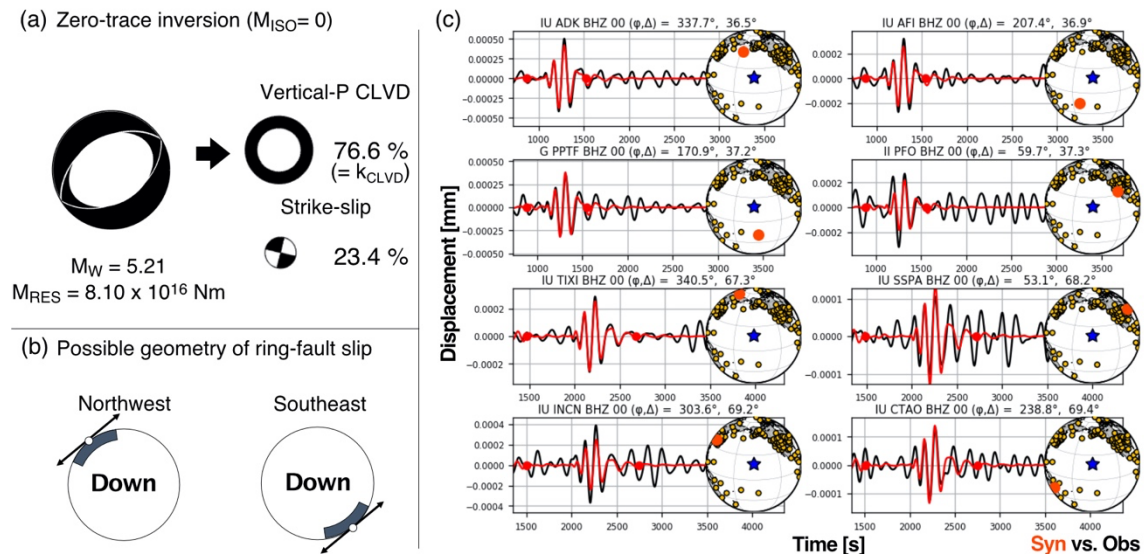


Figure S15.

Figure shows the inversion results for collapse event 17 using teleseismic waves filtered at 100 – 200 seconds: **(a)** inversion assumes zero trace ($M_{ISO} = 0$), yielding a ring-fault slip of $M_{RES} = 8.10 \times 10^{16}$ Nm ($M_W = 5.21$) with 76.6% vertical-P CLVD and 23.4% strike-slip; **(b)** Based on the inverted P-axis direction and the CLVD ratio (k_{CLVD}), the ring-fault slips partially along either the northwest or southeast corner of the caldera. **(c)** Plots show comparison of teleseismic waveform between data recorded at representative global stations and synthetics.

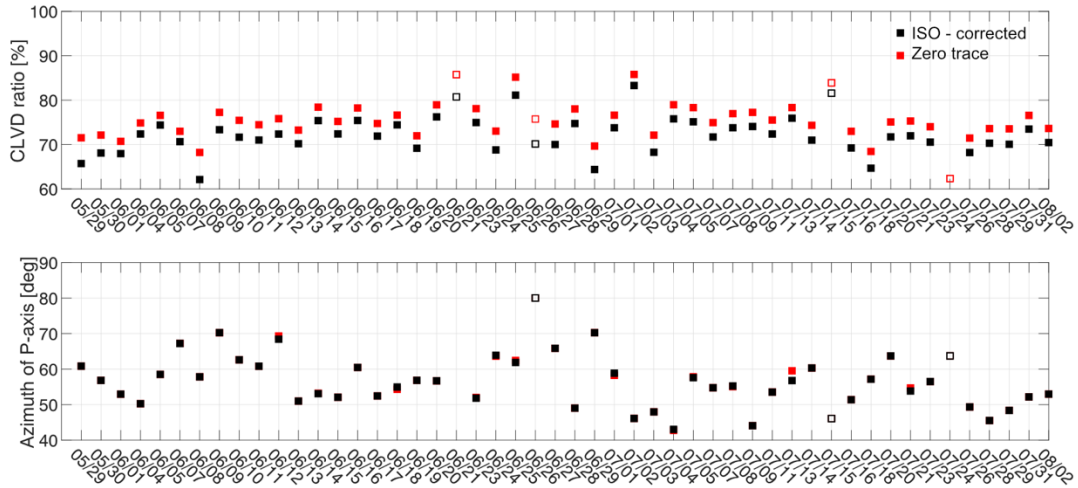


Figure S16:

Figure shows the CLVD ratio k_{CLVD} (top) and the azimuth of the P-axis from the strike-slip component (bottom) of the inversion results for the later 50 collapse events between 05/29 and 08/02. Results from the preferred inversion with isotropic correction (black) and inversion with zero trace constraint (red) are fairly similar. k_{CLVD} is between 65 and 80%, indicating partial collapse on ring fault with arc angle $< 90^\circ$. The average azimuth of the P-axis is 60 degree away from the north, indicating the slip occurs along either the northwest or southeast corner of the ring fault. Inversion results performed with less than 20 seismic records are unreliable and marked by unfilled squares.

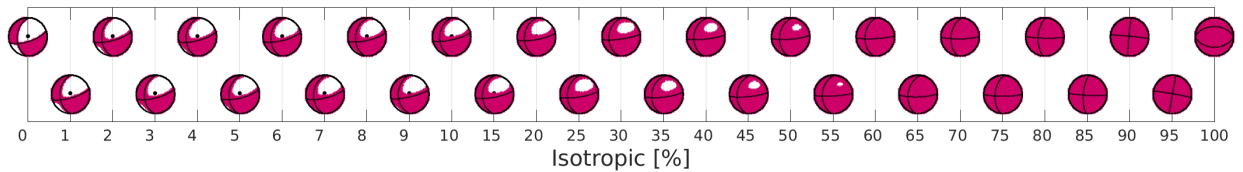


Figure S17:

Figure shows the fit of antipodal PKIKP (from Butler, 2019; marked with a black dot) with focal mechanisms generated for a range of isotropic contribution. The CLVD contribution is fixed at zero. The only solutions that match with the dilatational polarity are solutions with very little isotropic contribution ($< 5\%$).

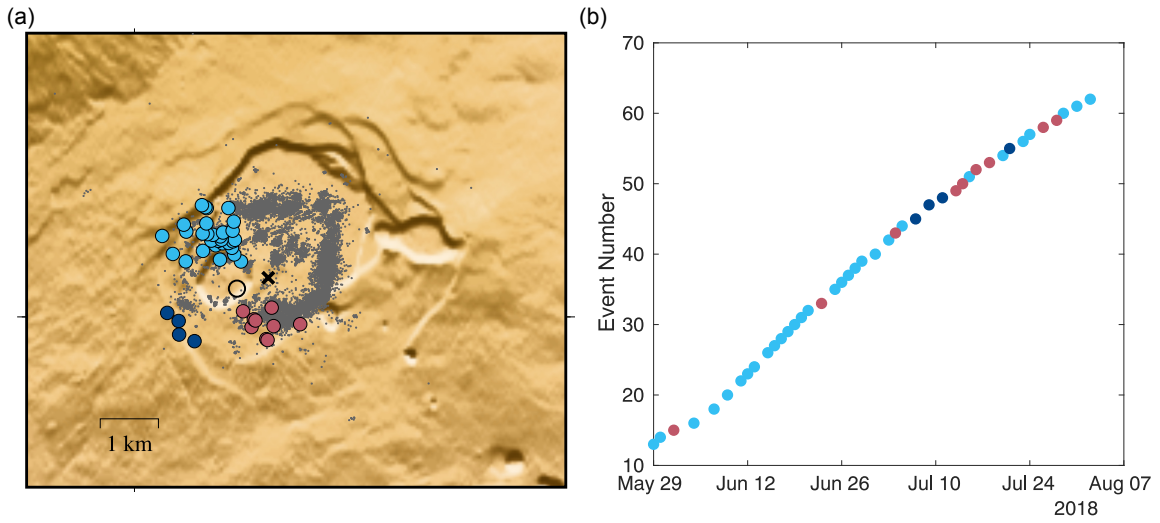


Figure S18:

(a) Map shows the location of the microseismicity cluster (grey dots) and large collapse events (colored circles) between 2018 May 29 and Aug 02 from Shelly and Thelen (2019). The circles are color-coded based on location. **(b)** Graph showing the event numbers and their respective location.

Data Set S1:

The csv file contains the moment tensor solutions for the early 12 explosive events and the 50 collapse events. The moments are given in N•m. Event 4 and 5 (marked with asterisk) have unreliable moment tensor solutions due to unusually long source duration.

Data Set S2: Moment tensor solutions for collapse events using global stations

The zipped file contains a Readme file and a catalog containing the teleseismic moment tensor solution with zero trace constraint for the 50 late collapse events (event 13 to 62). Both total and resolvable seismic scalar moments are provided for completeness but only the resolvable seismic scalar moment is reliable.